Status and perspectives of crystalline-silicon photovoltaics in research and industry

Christophe Ballif[a], Franz-Josef Haug[a], Mathieu Boccard[a], Pierre J. Verlinden[b,d,e,f], Giso Hahn[c]

[a]Photovoltaics and thin film electronics laboratory (PV-Lab), Institute of Microengineering (IMT), Ecole Polytechnique Fédérale de Lausanne (EPFL), Rue de la Maladière 71b, CH-2000 Neuchâtel, Switzerland
[b]AMROCK Pty Ltd, PO Box 714, McLaren Vale, SA 5171, Australia
[c]Photovoltaics Division, Department of Physics, University of Konstanz, Universitätsstraße 10, D-78464 Konstanz, Germany
[d]School of Photovoltaic and Renewable Energy Engineering, University of New South Wales, Sydney, Australia
[e]Institute of Solar Energy, Sun Yat-Sen University, Guangzhou, China
[f]State Key Laboratory of PV Science and Technology, Trina Solar, Changzhou, Jiangsu, China

Abstract

Crystalline silicon (c-Si) photovoltaics has long been considered energy intensive and costly. Over the past decades, spectacular improvements along the manufacturing chain have made c-Si a low-cost source of electricity that cannot be ignored anymore. Over 125 GW of c-Si modules have been installed in 2020, 95% of the overall photovoltaic (PV) market, and over 700 GW have been cumulatively installed. There are some strong indications that c-Si photovoltaics could become the most important world electricity source by 2040-2050. In this Review, we survey the key changes related to materials and industrial processing of silicon PV components. At the wafer level, a strong reduction in poly-silicon cost and the general implementation of diamond-wire sawing has reduced the cost of monocrystalline wafers. In parallel, the concentration of impurities and electronic defects in the various types of wafers has been reduced, allowing for high efficiency in industrial devices. Improved cleanliness in production lines, increased tool automation, improved production technology and cell architectures all helped increase the efficiency of mainstream modules. Efficiency gains at the cell level were accompanied by an increase in wafer size and by the introduction of advanced assembly techniques. These improvements have allowed a reduction of cell-to-module efficiency losses and will accelerate the yearly efficiency gain of mainstream modules. To conclude, we discuss what it will take for other PV technologies to compete with silicon on the mass market.

Summary

Crystalline silicon is today's main photovoltaic technology, enabling to produce electricity with minimal carbon emissions and at an unprecedented low cost. This review discusses the recent evolution of this technology, the present status of research and industry, and the near future perspectives.

This version of the article has been accepted for publication, after peer review but is not the Version of Record and does not reflect post-acceptance improvements, or any corrections. The Version of Record is available online at: https://doi.org/10.1038/s41578-022-00423-2

Introduction

Photovoltaics is a major actor of the ongoing energy transition towards a low-carbon-emission society. The photovoltaic (PV) effect relies on the use of a semiconducting material that absorbs light and converts it to free electrical charge carriers. Although several materials can be—and have been—used to make solar cells, the vast majority of PV modules produced in the past and still produced today are based on silicon—the second most abundant element after oxygen in the Earth crust—in a crystalline form. In addition to a fast increase in volume manufacturing, one explanation for the success of crystalline (c-)Si technologies in recent decades can be found in the easy way the manufacturing chain for c-Si from quartz to module can be split in separate steps (Fig. 1a). The perceived disadvantage of the numerous processing steps in c-Si PV technology compared to the easier processing of thin films has turned over the years into an advantage: each step can be, and has been, optimised quasi-independently with high volumes and high yields (typically >98% from wafer to cell), leading to significant cost reductions at all steps (Fig. 1b) as new manufacturers often focus on only one or two steps in the value chain — wafer, cell or module manufacturing, or system installation — instead of trying to consolidate the profit margins by vertical integration.

The history of Si photovoltaics is summarized in Box 1. Over the past decade, an absolute average efficiency improvement of 0.3-0.4% per year has taken place, both for monocrystalline and multi-crystalline Si (Fig. 1c). The efficiencies of modules sold in 2021 typically range from 17.4% (low-grade multi-crystalline cells) to 22.7% (high-performance back-contacted cells) [1] with an estimated average of 20% for the most produced technology (passivated emitter and rear cell, PERC, monocrystalline). Note that because of fast-evolving module designs, but also because existing lines are still being depreciated, the average efficiencies are lower than the state-of-the-art efficiencies. The newest mainstream, large modules will have efficiency values above 21%, but older-generation modules are still being produced with an average efficiency of 19%. Highest-efficiency modules (>22%) can require significantly more complex manufacturing, which increases their cost and price by a factor of two to three. They are thus mostly relevant for niche applications (such as rooftop or remote systems) for which the efficiency and power density are more important than the levelized cost of the produced electricity.

The question of whether efficiency improvements and cost decreases will keep their pace is crucial for the prospects of photovoltaics as a global energy source. In this Review, we explain why and how this trend is likely to continue, based on a detailed analysis of the evolution of the material technology and present trends in research and development.

We start by reviewing the key elements that have enabled silicon photovoltaics to become a low-cost source of electricity and a major actor in the energy sector. Material usage reduction and wafer quality improvement, jointly with a spectacular price decrease were simultaneously achieved in the past decades. We then discuss how the industry's favourite cell technology has evolved in the past few years from the historical structure described in the 1970s towards a better-performing PERC structure. We further discuss how, following the demand for high-performing and low-cost PV systems, even more efficient cells relying on passivating contacts are currently being rapidly developed with strong industrial involvement. We then survey the recent evolution of modules that enabled a reduction of cell-to-module efficiency losses, particularly in the past couple of years. Over the past decade, mainstream module efficiency increased by 0.3-0.4% absolute per year on average,

reaching now efficiencies of 19-22%. The improvements discussed here notably enable today's modules to generate the energy needed to fabricate them in much less than one year. Based on present-day knowledge, we describe the technological innovations that will enable the cost of PV electricity to routinely reach US$ cts 1.3-3 /kWh within the next decade all around the globe. Finally, we briefly discuss how alternative PV technologies could compete with silicon on the mass market.

From polysilicon feedstock to wafers

For high-efficiency PV cells and modules, silicon crystals with low impurity concentration and few crystallographic defects are required. To give an idea, 0.02 ppb of interstitial iron in silicon, corresponding to a concentration of around 10^{12} cm^{-3}, can bring a c-Si solar cell efficiency from 20% down to ~ 12%, as excited electrons lose their energy to iron-related recombination centres. The required purification of the silicon feedstock and cleanliness of the following processes are comparable to specifications in microelectronics.

Silicon processing starts with metallurgical-grade silicon (with ~1% impurities), which is reacted with HCl to create trichlorosilane ($SiHCl_3$, or TCS), a liquid with a boiling point of 32 °C. A series of distillation cycles (typically 3-5) is used to obtain TCS with a purity of 9N to 12N, that is, with less than one impurity per billion atoms (one per trillion in the 12N case). Subsequently, TCS is fed together with H_2 into a cooled-wall reactor, in which high-purity silicon filaments (a few millimetres in width) are heated to 1150 °C. TCS dissociates thermally at the surface of the hot silicon filaments, and silicon deposition thickens the filaments to rods of 10-20 cm in diameter. This process, usually called Siemens process, is a costly and energy-intensive part of the silicon PV chain, but improvements in internal jar reflective coatings and increases in reactor size reduced its cost and energy requirements. Up to 10 tons of high-purity silicon can now be produced in ~100 hours in the largest reactors, with an energy consumption of 35-45 kWh/kg [2]. The silicon rods are then crushed into chunks and used for the growth of silicon ingots. Depending on the number of distillation cycles, which impacts the material quality, the price of solar-grade silicon was typically in the range of US$ 6-7 /kg for low-quality silicon, and up to US$ 10-12 /kg for high-quality silicon in 2020. Further cost reduction is possible [2], for instance by using larger tubular silicon filaments, which reduce the deposition time thanks to their increased initial surface area [3]. Fluidized bed reactors constitute an alternative approach to deposit silicon and could halve the energy needs for this step [4], but they have a small market share [5]. With state-of-the-art processes and starting from sand, the total electricity consumption to produce one kg of purified polysilicon feedstock amounts to about 60 kWh (11 kWh/kg for making metallurgical-grade silicon, 49 kWh for purifying and producing polysilicon).

Two principal techniques are then used for the preparation of silicon ingots (Box 2): directional solidification (DS) and the Czochralski (Cz) method [6], [7], with the Cz method using roughly 4 times more electricity than the DS technique (32 versus 7 kWh per kg of crystallised silicon). Blocks and ingots are subsequently cut into (pseudo-)square bricks with typical edge lengths of 156-210 mm, and then sawn into wafers using the multi-wire sawing technique. Here, a thin steel wire is wound multiple times around guiding cylinders to saw simultaneously up to several thousand wafers. The original process developed in the 1980s used a slurry of silicon carbide particles in glycol solution to chip through the silicon [8]. This process had significant kerf losses (the wire diameter plus twice the diameter of the silicon carbide particles), adding up to 120-200 µm. Between 2015 and 2019,

diamond wires (steel wires bonded with microparticles of diamond) became the new standard [9], reducing kerf losses to 50-70 µm and significantly contributing to the reduction of wafer price in recent years. Combined with reduced cell thickness and increased cell efficiency, the amount of raw silicon decreased spectacularly from 14 g/W in 2000 to 3.0 g/W today (Fig. 1d, all power values refer to peak power under standard test conditions). Summing up all electricity consumption for going from sand to wafer yields just under 100 kWh/kg (including 5 kWh/m^2 for wafer sawing), that is, 0.3 kWh/W. This energy expenditure is compensated in the field in 2 to 4 months depending on the irradiance. Altogether, the energy payback time for silicon PV systems amounts nowadays to less than a year in Southern European countries (1.2 years in northern Europe) for a standard mounting for both DS and Cz growth technologies, with a slight advantage for silicon grown by DS due to the lower energy requirements [10], [11], and is well below one year considering only the module part.

As a result, the cost of silicon wafers per m^2 of module area is now astonishingly low compared to just ten years ago. With a typical wafer thickness of 170 µm, in 2020 the selling price of high-quality wafers on the spot market was in the range of US$ 0.13-0.18 per wafer for multi-crystalline silicon and US$ 0.30-0.35 per wafer for monocrystalline silicon, which, with a typical size of 158.75x158.75 mm^2, corresponds to US$ 6-13 /m^2. This price sets a high benchmark for the alternative wafering techniques discussed in Box 2. Noticeably, a strong demand for Si feedstock has led to a sharp price increase in 2021 by a factor 2 to 3, Together with a PV glass shortage, this has contributed to a price increase along the full chain of PV, which is anticipated to come down again in 2022 and 2023 with the addition of new capacity.

Carrier lifetime in silicon

The indirect bandgap of silicon yields only a moderate absorption and thus requires a wafer thickness of 100-200 µm to absorb most of the light with energy above the bandgap. For the photo-generated minority carriers to diffuse towards the selective contacts with a minimum of recombination losses, the (effective) minority charge carrier diffusion length L_{eff} should be several times larger than the thickness of the wafer; L_{eff} is defined in terms of the minority charge carrier diffusivity D and the effective excess charge carrier lifetime τ_{eff} as $L_{eff} = \sqrt{D \cdot \tau_{eff}}$. Long lifetimes require a low level of recombination losses.

The recombination losses come from the bulk properties (Box 3), but also from dangling bonds at the surfaces. Through chemical surface passivation, these dangling bonds can be bonded with other atoms, for example with oxygen when the surface is passivated with silicon dioxide. Hydrogen also passivates dangling bonds very effectively. However, hydrogen passivation can be unstable under heat or UV light. By contrast, field-effect surface passivation relies on layers with suitable polarity of fixed charges (positive charges for n-type surfaces, such as SiN_x, or negative charges for p-type surfaces, such as Al_2O_3), which accumulate majority carriers and deplete the surface of minority carriers through band bending, thus reducing recombination by removing one type of carrier from the surface [12]. Surface passivation can in principle also be achieved by inversion, but this type of passivation is less efficient than accumulation, is more sensitive to charge variations, and can be destroyed when the layer is locally opened for contacting due to parasitic shunting [13], [14].

Increasing effective lifetime during processing

The density of defects within the wafer bulk can significantly change during solar cell processing. Depending on processing temperatures, precipitates can be dissolved or formed depending on their solubility and diffusivity [15], and gettering processes can remove transition metals by attracting and collecting them into "sinks" with higher solubility [16]. Internal gettering refers to segregation in extended defects or highly doped regions, whereas external gettering utilizes layers at the wafer surface such as a doping glass [17] or a SiN_x:H layer [18].

Besides its role in surface passivation, hydrogen also has a positive impact on bulk recombination. It can be introduced by a H-rich SiN_x:H layer deposited by plasma-enhanced chemical vapour deposition (PECVD), followed by a short annealing (firing) to release the hydrogen into the bulk silicon. Hydrogenation is effective in improving areas of higher defect density, conveniently supporting the improvements achieved by gettering, although the local defect structure is very important [19]. Hydrogenation was also found to improve τ_{eff} more effectively in cleaner samples, especially when reducing the recombination activity of grain boundaries [20]–[22].

Bulk lifetime degradation phenomena

Reaching a high τ_{eff} at the end of the solar cell fabrication process is important, but it is not sufficient to ensure a long-lasting and efficient solar electricity production. For example, boron-doped p-type c-Si with high oxygen concentration, such as in a Cz material, is vulnerable to degradation under illumination [23]. This effect reduces τ_{eff} within several hours of carrier injection; it scales almost linearly with boron concentration and roughly quadratically with interstitial oxygen concentration [24], [25]. This process was termed boron-oxygen (BO)-related light-induced degradation (LID), which is misleading because it also occurs under biasing of cells in the dark, as only the presence of excess charge carriers is needed, not the photons themselves. A fundamental lifetime limit imposed by BO-LID was established by studying bulk lifetime after full degradation [26]. In 2006, it was discovered that lifetime after BO-LID can be regenerated by a process involving excess charge carriers at 150–300 °C in the presence of hydrogen in the sample [27], [28]. The kinetics of the degradation–regeneration cycle can be described by a three-state model (annealed, degraded, and regenerated state) [29] and more generalized models [30]. The defects can be deactivated by exposure to a high light intensity at above 200 °C for less than 1 min [31], [32] or by biasing the cell at around 200 °C in the dark (for example in a stacked configuration) [33], [34]. The deactivation is stable long-term, thus, BO-LID is no longer the dominant limitation of boron-doped Cz silicon solar cells. Additionally, gallium almost completely replaced boron for fabrication of p-type wafers, thus avoiding BO-LID issues, even though gallium distribution in the ingots is less homogeneous than boron distribution [35].

Another degradation mechanism in bulk silicon, discovered in 2012 [36], occurs on measurable timescales only above room temperature mainly in p-type materials. Therefore, it was termed LeTID (light- and elevated-temperature-induced degradation). Similar to BO-LID, it is based on the presence of excess charge carriers, but does not have a clear dependency on doping or oxygen level [37], and a regeneration can be observed, too. The effect is more pronounced in multi-crystalline

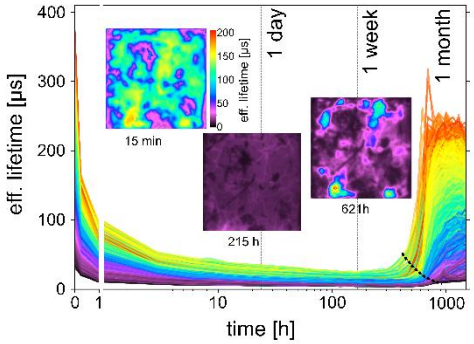

material [36] (a) b)

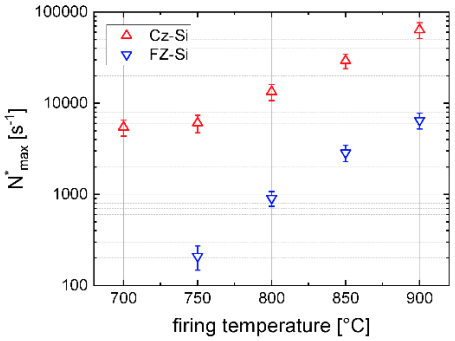

Fig. *2*a), where its strength can be influenced by gettering and the local defect structure [38], [39], but it is also observed in Cz (including gallium-doped) and even higher-purity float-zone (FZ) material

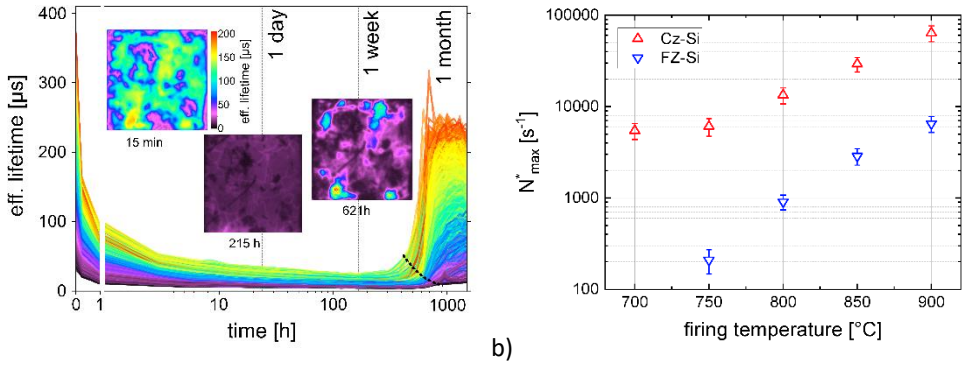

[40], [41] (a) b)

Fig. *2*b). Recently, LeTID was also reported for sample structures based on n-type wafers, provided they contain highly doped p-type or n-type layers [42], whereas samples with moderate n-type doping seem to be unaffected [41]. The presence of hydrogen in the silicon bulk is presumed to be a prerequisite for the defects to form [43], and peak firing temperatures and ramping rates have a

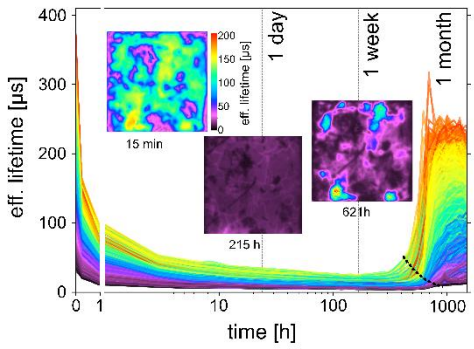

strong impact on the strength of LeTID [39], [44] (a) b)

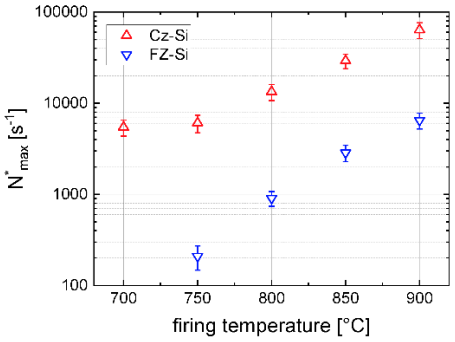

Fig. *2*b). Early models assumed that a diffusing species is involved in the process [44]. More recent findings resulted in a four-state model with a 'reservoir' state determining the availability of defect precursors for degradation [45]. Possible measures to avoid LeTID in p-type solar cells are the use of lower firing temperatures or thinner wafers [44], although neither one appears to be compatible with current industry needs. Thermal treatments in the dark or under carrier injection might be more suitable for implementation in mass production. As regeneration timescales are longer than for BO-LID, LeTID remains a severe problem for p-type solar cell processing. Many manufacturers found mitigation strategies resulting in reduced degradation strengths [46], but all need extra steps and/or increase processing cost.

The vulnerability of p-type silicon to these degradation phenomena brought back the 60-year-old discussion about whether p-type or n-type silicon is better suited for solar cell production. Early silicon cells were made on n-type wafers, but when space applications became a large market, p-type silicon was favoured because of a better resistance to electron irradiation in orbit. Subsequently, p-type remained the substrate of choice, mostly because the rear metallisation with aluminium conveniently forms a contact and a back-surface field (BSF) simultaneously. However, long lifetimes are easier to reach with n-type material and most cells with high efficiency (>23%) rely on long bulk lifetimes (>1 ms) [47]. In terms of processing, solar cells based on n-type silicon show a slightly higher complexity and higher manufacturing cost, as both phosphorus for the BSF and boron for the emitter (the region of the wafer showing opposite doping from the bulk [48]) have to be diffused, and because both front and rear metal layers require silver-based pastes. The boron-doped emitter might also cause problems, because its formation might generate oxygen-related defects. This issue can be avoided by a pre-processing step at high temperature, typically more than 1000 °C, to dissolve oxygen precipitates (called 'tabula rasa') [49], but at the cost of adding process complexity, which prevents its use in industrial production.

Solar cell processing

Most silicon solar cells until 2020 were based on p-type boron-doped wafers, with the pn-junction usually obtained by phosphorus diffusion, and until 2016 they were mostly using a full-area Al-BSF (Fig.3a), as first described in 1972 [50]–[52]. Since then, constant cost decrease and efficiency increase followed from multiple small but important improvements. The main ones are screen-printing of metal contacts, effective surface textures, positively charged silicon nitride surface passivation and selective emitters.

A major challenge in c-Si technology consists in applying metallic electrodes to extract the charge carriers. Because of the high defect density at direct metal/semiconductor interfaces, the contacts are an important source of recombination. There are two main options to limit their impact, giving rise to the various device structures illustrated in Fig. *3*.

The first option is to reduce the metal/Si contact area. The remaining metallised areas should have low contact resistivity, and the surface between the contacts should be passivated [53], [54]. Using photolithography to define the coverage fraction and controlling the doping profile in the adjacent regions in the wafer, this concept resulted in the first silicon solar cell with a 25% designated area efficiency in 1999 [55]. Usually called PERC following Ref. [56], a simplified version of this design, shown in Fig. 3b, is at the heart of current mass production.

The second option is to separate the metal electrode from the Si wafer. In this case, a stack of a passivating film (to reduce the density of interface defects) and a doped film (to selectively conduct only one polarity of charges) are inserted between silicon and the metal. Balancing the passivation characteristics and the contact resistance is the most difficult aspect of these 'passivating contacts'. The most widely used stacks consist of intrinsic and doped amorphous silicon (Fig. 3g,h) [57], or of silicon oxide and polysilicon (Fig. 3e,f) [58]–[60]. Passivating contacts have enabled the most recent record efficiencies beyond 25% [61].

Al-BSF cell processing

The typical industrial Al-BSF cell processing, predominant until 2017-2018, is presented in the left part of Fig. 4. Starting with boron-doped p-type wafers, a light-scattering texture is etched by wet chemistry. For monocrystalline wafers with (100) crystallographic orientation, random upright pyramids are obtained by anisotropic etching in caustic solutions, whereas for multi-crystalline material, isotropic etching in acidic solutions yields hemispherical pits. Next, the n-type emitter is formed using a $POCl_3$-based phosphorus diffusion at around 800-850 °C, generally in quartz tube furnaces with batches of about 1200 wafers that are loaded back-to-back. The phosphorus atoms diffuse less than 0.5 µm into the Si bulk with a diffusion profile that is optimised as a trade-off between lateral conductivity and emitter recombination. The phosphorus-silicate-glass layer formed at the surface of the wafer during the diffusion and the parasitic P-diffused region at the rear are etched away using wet chemistry. During the same etching step, the rear surface is chemically planarized. Next, PECVD is used to deposit a SiN_x:H layer on the emitter, where it acts as an anti-reflective coating and as a positively charged surface passivation layer.

Subsequently, a multi-step screen-printing process is used to form the metal contacts. First, a silver paste is screen-printed to form the soldering pads at the rear of the cell. After drying, the rear surface is printed with an aluminium paste that may contain additional boron. After drying and flipping the cell, the front surface is printed with a paste that contains silver and glass-frit to form

the front metallization. The next processing step is the co-firing in a belt furnace at a peak wafer temperature of around 800 °C, where several things happen simultaneously. On the rear of the wafer, aluminium melts and dissolves silicon. During cool-down, silicon recrystallizes according to the Al/Si phase diagram [62], incorporating aluminium and boron (if added to the paste) with concentrations up to their solubilities in the solid. This forms a highly-doped p-type BSF region. The remaining aluminium eventually solidifies to form the rear contact. On the front side, the glass-frit etches through the SiN_x:H layer, enabling contact formation between the silver and the highly-doped n-type emitter surface [63]. Another important phenomenon during co-firing is the release of hydrogen from the SiN_x:H layer. Hydrogen can passivate the numerous dangling bonds at the c-Si/SiN_x:H interface, as well as some crystal defects in the bulk of the silicon wafer.

Finally, current-voltage measurements are performed in the dark and under “one sun” illumination; this last measurement enables the extraction of the conversion efficiency and of the main parameters of the cell: the open-circuit voltage, V_{oc}, the short-circuit current, I_{sc}, and the fill factor, FF, which is defined as the maximum power output divided by the product of V_{oc} and I_{sc}. The reverse current-voltage characteristics and the reverse breakdown voltage are also tested. The cells are then sorted in a matrix of bins as a function of their efficiency and short-circuit current with company-dependent strategies. In most high-quality industrial production lines, the electroluminescence image of every cell is recorded and checked for micro-cracks or other defects, and the cells are additionally sorted by colour variation.

Evolution towards PERC and other designs

A first evolution introduced into industrial Al-BSF cell manufacturing around 2005-2010 was a selective emitter design [64]. This design includes a heavily doped emitter under the metal contacts and a lightly doped emitter between the metal contacts. Selective emitters simultaneously enable a good electrical contact and a low average emitter recombination. They are manufactured either by using a laser doping process that enhances doping under the contacts, or by an etch-back process in the area between the contacts. Significant progress was made over the past decade on silver pastes, and new formulations enable good contacting of very lightly doped emitters, which, combined with narrower line printing (currently less than 40 µm), reduces recombination in the emitter region [65] and at its surface. The main limitation of Al-BSF solar cells is thus nowadays recombination at the full-area rear contact, which limits their efficiency to just above 20% [66].

The PERC architecture (Fig. 3b) lifts this barrier by adding three processing steps (Fig. 4). First, after the emitter diffusion and surface cleaning/back etching, a thin (<2 nm) thermal oxide is grown on both sides of the wafer to improve the surface passivation (not shown on the figure). Second, a thin (<20 nm) Al_2O_3 and a thicker SiN_x:H layer are deposited on the rear of the cell, either by PECVD for both layers, or using atomic layer deposition (ALD) for Al_2O_3, and PECVD for SiN_x:H [67], [68]. Third, the dielectric passivation at the rear is locally opened by laser ablation--- recent developments in laser technology helped a lot with the industrialization of this process---before screen-printing of the aluminium paste, either full-area or only in finger shapes over the ablated regions for bifacial solar cells. The two main benefits of the PERC design are reduced rear side recombination, which results in an increased open-circuit voltage, and improved rear reflectivity, which results in an increased short-circuit current (Fig. 5a).

The first efficient cell based on the PERC concept was demonstrated at the University of New South Wales in 1989 [56], [69], [70], using FZ wafers and photolithography-intensive processing. It took over 20 years of collaborations between equipment makers, industry and research institutions to make a cost-effective solar cell form this innovative concept, enabling commercialization of PERC modules in 2010.

As a result of reduced rear recombination, bulk recombination emerged as the main limitation of the PERC cell, triggering interest in high-quality monocrystalline wafers. Unless gallium doping is used, the boron-oxygen defect is deactivated in an additional step that involves stacking cells onto a carrier that travels through a belt furnace at around 200 °C while maintaining a high forward electrical current through the series-connected cells in the stack. The high temperature and the high carrier concentration injected in the silicon cells increase the diffusivity of hydrogen in silicon. Because the efficiency gain outweighs the cost of the additional processing steps, a fast industrial transition from Al-BSF to PERC took place between 2016 and 2020. At the end of 2020, more than 70% of the cell market was PERC technology, and 80% of the wafer market was monocrystalline Cz wafers [10], [71], thus merging the weighted average of Fig. 1c into one single curve towards monocrystalline material. The industrial PERC process enables significantly higher efficiencies, 22-23% on average for monocrystalline Si, with typical record values around 23.5% for a full wafer made on production lines [72]–[74]. Higher values were reported (for example 24.0% from Longi Solar [75], Fig. 4b), but without clear indication about the exact contact structure or fabrication environment. Because it contains a local Al-BSF, the industrial “PERC” cell is strictly speaking a mixture of the PERC and PERL (passivated emitter, rear locally diffused) [76] solar cell concepts. But because this local Al-BSF is alloyed and not diffused, the cell is neither a pure PERC nor a pure PERL cell.

An alternative industrial c-Si cell architecture is the passivated emitter, rear totally diffused technology (PERT, Fig. 3c,d) [77]. This design is particularly interesting for n-type substrates, for which the combined formation of Al-BSF and Al contact is not possible. Instead, it includes both boron diffusion and phosphorus diffusion processes. Owing to their wafer polarity, n-type PERT cells are less prone to boron-related degradation effects, and have a higher efficiency potential than p-type PERC cells, owing to a lower sensitivity of the bulk lifetime to some metallic impurities. However, the process complexity is higher and the substrate can be more expensive if a higher initial lifetime is requested.

Shadowing by contacts on the front can be avoided by putting both contact polarities on the rear-side of the cell in an interdigitated back contact design (Fig. 3h,i) [78]. With this design--and with the use of the passivating contacts described in the next section--the two highest reported designated-area efficiencies are 26.1% for a p-type substrate [79] and 26.7% for an n-type substrate [80]. Back-contacted cells with remarkable total-area efficiencies around 25.0% are successfully commercialized by SunPower Corp. in their high-efficiency modules. Nevertheless, all solar cells with efficiency higher than 25% come at the cost of more complex processing, for example using photolithography for the definition of the contacts [81]. An important research trend is therefore to develop simpler process flows for cell efficiencies above 25% [82]–[84].

High-temperature passivating contacts

In PERC and PERT solar cells, metal contacts silicon locally on both sides. This leads to significant recombination, limiting the open-circuit voltages. This problem of 'classic metallisation' is evident when looking at the highest efficiencies for different cell architectures summarized in Table 1. This issue triggered interest in developing passivating contacts, consisting of a layer stack suppressing defects at the silicon surface yet ensuring the selective collection of charges towards the metallic electrode. Inspired by the improved properties of Schottky diodes that use a metal-insulator-semiconductor structure rather than a metal-semiconductor one, metal-insulator-semiconductor structures were suggested for solar cells in 1972 [85]. By 1983, open-circuit voltages as high as 695 mV were demonstrated and, to enhance the compatibility with high-temperature processing, it was proposed to replace the metal by degenerately doped silicon [86]. To improve the efficiency, some research labs still included a slight phosphorus diffusion at the front. In parallel, inspired by research on bipolar transistors with polysilicon emitters, other research teams developed cells using semi-insulating polysilicon [58]. Passivating polysilicon contacts (Fig. 3e,f) became popular after 2010, as they provide surface passivation and tolerate high processing temperatures. They are thus compatible with well-established gettering, metallisation and hydrogenation processes and, when applied to the full surface, provide good conductivity without crowding the photocurrent into small contact areas [87]. Thus, high-quality monocrystalline wafers and full-area polysilicon contacts form a potentially winning team.

Sandwiched between the wafer and the polysilicon film, a thin layer of silicon oxide has the pivotal role to balance surface passivation and contact conductivity. This oxide layer can be grown chemically [88], a process attractive for industrialisation because it can be integrated easily into the wafer-cleaning procedure. The oxide grown this way is generally only 1.0-1.5 nm thick, that is, thin enough for charge carriers to tunnel from the wafer to the polysilicon [89]. Alternatively, thermal growth of oxides is a standard step in semiconductor processing. The resulting oxides are generally thicker and more stoichiometric, thus insulating. To establish electrical contact, increasing the thermal budget of subsequent processing steps can be used to open conductive pinholes [90]–[92]. A layer of highly doped polysilicon can be obtained by low-pressure chemical vapour deposition (LPCVD) of an intrinsic layer and subsequent dopant implantation [79] or diffusion [93]. In-situ doping is also possible. Alternatively, doped amorphous silicon layers are grown by PECVD [87] or sputtering [94], and subsequently annealed to crystallize them and activate their dopants. Finally, a hydrogenation treatment is commonly applied to passivate defects in the interfacial oxide or at its interface with the silicon wafer.

Different acronyms have been used to name this contact technology. The most commonly adopted one is TOPCon (for tunnel oxide passivated contacts [95]), which we use here. Most recent research focuses on n-type polysilicon passivating contacts on the rear side of n-type silicon substrates, using a full-area metallisation of evaporated silver. Combined with a boron-diffused junction at the front, the highest reported efficiency for a small-area laboratory cell to date is 25.8% (26% with a rear junction configuration on a p-type wafer) [96]. For upscaling to commercial wafer-size, the rear side is generally contacted with an industrial metallisation: a layer of SiN_x:H is deposited followed by screen-printing of a metal grid. In a subsequent firing step, the paste etches through the SiN_x:H to contact the polysilicon film, and hydrogen released from the SiN_x:H passivates interfacial defects. To avoid the metal damaging the oxide layer, the polysilicon thickness has to be over 200 nm [93], [97].

Similar concepts were followed by various industrial manufacturers towards a mass production of n-type cells with passivating rear contacts [60], [98]. For example, 6" industry cells (Fig. 3f) displayed efficiencies of up to 25.25%, and an average efficiency of more than 23.5% in production lines, typically resulting in modules with efficiencies of up to 22.5% [84], [99]–[101].

For p-type wafers, the highest reported cell efficiency to date is 26.1%, obtained combining passivating contacts of both polarities and an interdigitated back contact design [79]. A 26.0% efficiency was reported for a p-type cell contacted on both sides, with a standard (non passivating) p-type contact at the front and a junction-forming n-type passivating contact at the rear [96]. The formation of p-type contacts is experimentally more challenging than that of n-type contacts, an effect attributed to the higher capture cross section of c-Si/SiO_2 interface states for electrons than holes [102], or to defect creation during the diffusion of boron atoms across the interfacial oxide [103]. The latter can be mitigated by using a boron-free buffer layer on the interfacial oxide [104], or by alloying the boron-doped layer with oxygen, which retards boron diffusion [105]. Alternatively, boron diffusion can be largely reduced by using a low thermal budget to crystallize the silicon layer, as is the case with rapid thermal annealing or co-firing [106].

The design of a high-efficiency solar cell with a TOPCon structure on both sides is still under development. The main difficulty is to combine high transparency, passivation and electrical conductivity on the front side. Current research trends to improve the front TOPCon transparency, besides reducing the thickness of the contact, include localizing the polysilicon only below the metal [107], replacing polysilicon with a more transparent material [108], or alloying polysilicon with oxygen or carbon. Both alloying strategies lead to a trade-off between transparency and conductivity [106], [109]. A second difficulty is the application of the TOPCon structure on a textured surface where, once again, p-type contacts are more problematic than n-type contacts [110], [111]. The best efficiency reached to date in a device with full-area TOPcon passivating contacts at the front and rear is 22.6% [112].

Low-temperature passivating contacts

An alternative route to form passivating contacts relies on hydrogenated amorphous silicon (a-Si:H). Intrinsic a-Si:H was found to provide a good surface passivation to c-Si as early as 1979 [113]. The ability to engineer efficient silicon solar cells using a-Si:H layers was demonstrated in the early 1990s [114], [115]. Many research laboratories with expertise in thin-film silicon photovoltaics joined the effort in the past fifteen years, following the decline of this technology for large-scale energy production. Their success suggests that strong synergies exist between the two fields [57], [116], [117], [80], [118], [119]. A key feature of such silicon heterojunction (SHJ) devices (Fig.3g,h) is their high V_{oc} (typically 730-750 mV, Table 1). Devices based on heterojunction structures hold the current world record for back-contacted cells at 26.7% efficiency [80] and for large-area wafer both-side contacted screen-printed cells at 25.3% efficiency [100], with a 2021 record of 26.3% with unspecified metallisation (c.f. Table 1). Several production lines report average efficiency in the range of 23.5-24.5% with silicon heterojunctions.

Among passivation materials, intrinsic a-Si:H has the peculiarities to be a single-phase material with a comparatively narrow bandgap (between 1.6-1.9 eV), to contain little to no fixed charge, and to provide excellent chemical passivation without any electric field [120]. The narrow bandgap induces small conduction-band and valence-band offsets between the crystalline silicon and a-Si:H. This

enables electrons and holes to flow out of the c-Si wafer through relatively thick layers (>10 nm) of a-Si:H without incurring severe resistance. This combination of electrical conductivity and outstanding chemical passivation makes a-Si:H unique and enables its use in passivating contacts.

Similarly to crystalline silicon, a-Si:H can be doped both n-type and p-type using phosphorus and boron. However, doping in a-Si:H is not as efficient as in c-Si, and the electron and hole densities are limited to less than 10^{19} cm^{-3} in both cases [121]. Because doping inherently creates defects in a-Si:H, doped layers deposited directly onto a c-Si wafer do not provide excellent passivation. Solar cell devices thus usually incorporate a thin (<10 nm) layer of intrinsic a-Si:H for surface passivation between the wafer and the doped a-Si:H layers [122]–[124]. This architecture was initially called heterojunction with intrinsic thin layer (HIT, now a Panasonic trademark) [114] and nowadays simply silicon heterojunction (SHJ). PECVD is the most used deposition method for a-Si:H layers, although hot-wire CVD [125] (and to a lower extent reactively sputtered) a-Si:H films also demonstrated passivation [126], [127].

Charge transport in a-Si:H is less efficient than in c-Si owing to the orders of magnitude lower charge mobilities. As a-Si:H contributes only negligibly to lateral transport of minority carriers towards the front metal grid, an additional transparent conductive oxide layer is typically required. Indium oxide alloyed with tin oxide is mainly used, although other alloying compounds and even indium-free alternatives exist [128]–[131], [119], [132]. Lateral charge transport also occurs in the wafer itself, which relaxes the constraint on the transparent conductive oxide. This is mostly true for electrons owing to the predominant use of n-type wafers, the higher mobility of electrons than holes in Si, and the higher contact resistance between the wafer and the electrode for holes, favouring the placement of the electron contact on the illuminated side of the device [133][133]. Approaches that do not include a transparent conductive oxide, although technically possible [134], [135], are not yet used, because direct metallization of a-Si:H films is delicate. Arguably, together with the wider bandgap, the low mobility of a-Si:H contributes to enabling very thin layers to efficiently ‘screen’ the influence of the electrode to ensure passivation and carrier selectivity [136], leading to highly efficient solar cells with a-Si:H stacks of about 10 nm on each side.

Optically, the small bandgap of a-Si:H induces parasitic light absorption when using a-Si:H as a window contact. Whereas all light absorbed in the doped layer is lost for photocurrent, part of the light absorbed in the intrinsic layer can contribute to the photocurrent [137]. The search for alternative contact layers providing improved transport and transparency is currently very active. Nanocrystalline silicon (showing a better transparency and doping efficiency than a-Si:H) and thin-film silicon alloys are natural directions for improvements [138]–[143]. Promising alternative materials include transition-metal oxides, but this research remains so far academic with an uncertain path for industrialization [144]–[150]. At this time, only MoO_x exhibits similar efficiencies as p-doped a-Si:H for the hole-selective contact, and TiO_x for the electron-selective contact [149], [151], [152]. In the latter case, a full-area aluminium layer acting as metal electrode contributes to the electron selectivity of the contact stack. The mandatory use of such metal electrodes in the case of electron contacts using non-silicon-based materials precludes their use on the light-incoming side of solar cells. Although an efficiency up to 23.1% has been demonstrated using a localized silicon-free electron contact [153], most of the highly efficient devices using metal oxides as passivating contacts still include an intrinsic a-Si:H passivation layer. This layer is so far required to reach excellent open-circuit voltages (typically >700 mV) with low-temperature approaches. Efficiencies

above 21% (two-side contacted) and 22% (all-rear-contacted) were demonstrated in 'dopant-free' architectures (not using doped silicon to form the contact) [154], [155]. Parasitic light absorption in a-Si:H is totally eliminated in interdigitated back contact devices, for which even light absorbed in a front intrinsic a-Si:H layer contributes to photocurrent [117], [154], [156]. This structure has enabled the highest-efficiency silicon solar cells since 2015 [117], [157]. Process complexity precludes industrialization, but significant simplifications of the manufacturing process were demonstrated [82], [83].

In all approaches involving a-Si:H, the post-a-Si:H processing steps must be kept below 200-250 °C: hydrogen effusion at temperatures above 200 °C leads to performance drop (mostly through loss of passivation). This effect can be mitigated [158], [159], and even reversed up to temperatures as high as 400 °C [160], but above 450 °C the passivation ability of a-Si:H is irremediably lost. Consequently, silver screen-printing pastes cannot be fired at high temperatures like in standard cell processing, instead requiring the use of low-curing-temperature pastes. This fundamental difference distinguishes SHJ contacts (also called low-temperature passivating contacts) from TOPCon contacts. Despite remarkable progress, the low-temperature silver pastes are still a factor two to three more resistive than high-temperature ones, resulting in a higher consumption of silver than for PERC cells with an equivalent metallisation pattern [161], [162]. However, multi-busbar or proprietary approaches such as SmartWire™ enable a reduction of the silver cost [83]. The limitation to low processing temperatures also prevents wafer-bulk improvement by high-temperature impurity gettering (except as an extra step before a-Si deposition [163]). Low processing temperatures, however, enable the use of thinner wafers compared to standard PERC technology, down to below 100 µm [57], [164], [165]. Originally, only n-type wafers with long carrier lifetime were considered for SHJ technology, but similar efficiencies have since been demonstrated for high-quality p-type and n-type wafers [116], [166], [167].

Minimizing cell-to-modules losses

Moving from individual wafers to full modules, there is a systematic difference between the module power and the sum of the power of individual cells. The ratio of these powers is called the cell-to-module (CTM) power ratio, and is usually around 95-97%. Similarly, the module efficiency is lower than the average cell efficiency, leading to a CTM efficiency ratio of typically 85-90%. The evolution over the past 20 years in wafer size, shape and interconnection is illustrated in Fig. 6. After decades of fairly standardized wafer and module sizes, 2019 saw a paradigm shift, with the emergence of larger wafers and more aggressive assembly techniques. This change in industry targets aimed at increasing the CTM efficiency ratio, as high module efficiency translates in savings on module costs and installation costs per W. Assuming a configuration with 5 busbars (Fig. 6b, 2017 design), mono-crystalline 156x156 mm^2 PERC cells with 22.44% efficiency would typically lead to a 60-cell module [10] sized 1.7 m^2 with 19.5% efficiency (Fig. 6a, top). Using the same cell efficiency but applying a module design illustrative of the trends of 2021 (210x210 mm^2 cells cut in three and reassembled with an improved interconnection scheme in a larger module of 2.4 m^2, Fig. 6b, 2021 design) can lead to state-of-the-art PERC modules with an efficiency of 21% (Fig. 6a, bottom), an increase of the CTM efficiency ratio from 87% to 93%.

Considering the importance of module design changes for increasing the efficiency, we describe here the origin of module losses and the mitigation pathways to reduce them. The factors contributing to

module losses are broken into 3 broad categories: geometric, optic, and electric factors (Fig. 6a), and their contributions are obtained using the software SmartCalc.CTM (www.cell-to-module.com).

The main CTM loss is geometric and originates from the non-unity coverage of cells in the module (the coverage is only ~90% of the total area for typical modules). This loss accounts for more than 1.5% of the absolute efficiency difference, but it is not accounted for when calculating power CTM loss, explaining its higher value. Optical losses are due to the reflection of light at the air/glass interface, to the differences in reflection between a cell in air and a cell embedded in the encapsulation, to absorption losses in the encapsulation, and to extra shadowing from interconnection ribbons or wires. Optical gains also occur, because part of the light reflected from the fingers, interconnection ribbons and back-sheet in the space between cells can be internally reflected at the glass/air interface, giving it another chance to be absorbed in the cells [168]. Finally, electrical losses come from the cells' electrical interconnection.

Improvements in the stringing of cells (series interconnection of multiple cells) enabled the move from typically two or three 1.5-mm wide busbars in 2012 to five or six 0.9-mm wide busbars in 2014. Most recent high-efficiency modules incorporate 9 to 12 busbars, or even up to 18 to 21 wires [169]. Although this increase usually does not change the CTM ratio, it shortens the finger length, which decreases series resistance at the cell level and enables the use of thinner fingers (resulting in lower silver paste consumption and lower shadowing), improving the cell, and thus module, cost and performance [170], [171].

Increasing the wafer size is attractive because it improves the productivity of cell and module lines and reduces the loss due to cell spacing in the module. However, larger wafers produce more current, which increases the electrical losses for a given interconnection. Cutting the cells in half reduces the interconnection losses by a factor four [172], [173]. Assembling a PV module with series and parallel interconnections from half-cut cells also makes the module more tolerant to partial shading and improves its reliability against hot spots [174]. Most of the PV industry has thus switched to larger size (with typically 166, 182 or 210 mm lateral wafer sizes) and half-cell modules in 2020. The cell cutting process is critical and must be tailored to minimize edge defects and maintain high performance, especially for high-efficiency devices based on material with long carrier lifetime and thus diffusion lengths. The significant series-resistance reduction at the module level can outbalance a moderate loss in cell efficiency upon cutting [175]. This effect is particularly marked in standard test conditions corresponding to full-sun illumination (thus for the rated module power), but is more questionable for lower illumination conditions, under which the decrease of series-resistance has less impact. Thus, the gain in performance is obvious for sunny locations, but smaller for temperate climates.

Innovative designs aiming at suppressing the gap between cells to improve module efficiencies are explored by many companies [176]. In the shingle design, the wafer is cut into multiple slabs along the edge of the busbars. Slabs are then assembled similarly to shingles on a roof, with each busbar hidden under the adjacent cell and the electrical contact formed by conductive adhesive (Fig. 6c, bottom). Challenges include reliability and yield, owing to the overlap of the cells [177]–[180], and silver paste consumption owing to the long fingers. An innovative tiling ribbon solution, potentially alleviating these limitations, was recently proposed by several companies. It uses half or third wafers

interconnected with multi-busbars that are flattened at the point of overlap [176], thereby creating a negative gap between consecutive cells (Fig. 6c, middle).

Noticeably, most commercial modules incorporate an anti-reflection coating on the glass, typically consisting of a porous glass layer with a low refractive index. This layer reduces the weighted solar reflection at the air/glass interface from 4% to about 1.3-2% for normal incidence, and higher benefits are obtained at oblique incidence angles [181], [182].

Inside the laminate, the light reflected by the interconnecting ribbons can be largely recovered if the surface of the ribbons is grooved and thus reflects light at an oblique angle, enabling total internal reflection at the glass/air interface and absorption in the cell. The rounded shape of wire interconnects--which are becoming standard--partly enables this effect.

Combining several approaches, optical gains can compensate optical and electrical losses, leading to CTM power ratios over 100% [175], [183]. Nevertheless, the CTM efficiency ratio always remains below 100%, mainly owing to the fact that the module area is larger than the total cell area. Overall, cost remains the main driver for large-scale production, and decides on the implementation of many advanced strategies that are already technologically demonstrated.

Continuous industry improvements

Average module efficiency is increasing by about 0.3-0.4% absolute per year, and this trend is accelerating with the transition to mono c-Si and novel module design [10] (Fig. 1c). Efficiency increases will continue in the coming decade, at the end of which the maximum practical efficiency for single-junction silicon modules (23-24% for mainstream and possibly 25% for high-end modules) should be reached through the sets of improvements we described (better material, improved passivation, better contacting pastes, modified/improved cell structures including passivating contacts, modified module assembly).

In parallel, reliability continues to be of paramount importance, as reducing the expected annual degradation rate lowers the calculated levelized cost of electricity. Based on past experience and accelerated testing, many manufacturers offer warranties of 25 or even 30 years on the product performance, usually within a linear (relative) degradation of typically 0.5-0.7% per year. Besides the aforementioned degradation of the bulk silicon material, c-Si modules are subject to various degradation modes. The potential difference between the (grounded) outside of the module and the wafers in high-voltage strings can lead to potential-induced degradation [184]–[186]; UV light induces yellowing of the polymers; thermal and mechanical stress can crack cells and interconnections; corrosion can degrade contacts; encapsulants can delaminate, and so on [187]. These effects can be minimized by either cell-level modification (for example using denser Si-rich silicon nitride layers to prevent potential-induced degradation) or module-level modifications, such as using encapsulating polymers and backsheets that are more resistive and more stable to UV light. Some technology-specific degradation mechanisms also exist. For example, a few studies have reported a slightly higher degradation rate for SHJ modules fabricated in the early 2000s than for modules made with standard multicrystalline BSF cells from the same period [188]–[191]. It can be expected that new technologies showing higher performance are more prone to degradation, thus requiring dedicated strategies for high reliability that were not necessary (thus not introduced) 5-10 years ago [192]–[194]. The maturation of such strategies will likely be hastened by the large-scale

industrial adoption of passivating contact technologies, enabling these modules to reach similar—or even improved—reliability compared to today's standard.

The International Electrotechnical Commission (IEC) testing standards, such as IEC 61215, define standard procedures to detect design and manufacturing flaws in PV modules. However, they are not designed to guarantee a 25 or 30-year lifetime of the module in every climate, as they do not reproduce accurately the reality in the field. Harder testing sequences, with longer cycles and stricter criteria (such as UV, heat, and current flow) are frequently used in the industry to give manufacturers better insurance that their warranty is valid, especially when changing materials or suppliers to achieve better efficiency or lower cost. Reliability testing must always remain a major concern when establishing large solar parks with investments of several hundreds of millions of dollars, and the science of reliability of PV modules is continuously developed to improve the predictability of failures [188], [195]. On a positive note, several evaluations of systems that are more than 20 years old show that most modules still perform well past their expiration date [195]. However, these old-technology modules were produced with very different materials and designs from today's standards, precluding a complete extrapolation of these results.

One such increasingly popular designs is bifacial modules. Such modules can provide more annual energy per rated W than monofacial ones by enabling light absorption from both sides. Bifacial modules are gaining a larger market share despite slightly higher manufacturing costs [196]–[198]. This bifacial gain, which is also valid for tracking systems, depends on the performance under back-side illumination. The bifaciality factor, the ratio of rear-illuminated efficiency to front-illuminated efficiency, ranges from 70%-75% for p-type PERC to 96% for n-type SHJ cells, and the additional energy yield, typically around 5%-15%, depends on the design and arrangement of the module arrays, on the location, and on the ground albedo.

In 2020, large solar power plants (>10 MW) can be installed for around US$ 0.5 /W in several countries, and solar electricity costs through power purchase agreements are reported below US$ cts 2 /kWh for large solar farms located in sunny countries and US$ cts 4.7 /kWh in Germany [199]–[201]. Anticipating further module cost reductions (-30% relative), module efficiency increases (+20% relative), and improvements in solar park mounting and configuration (bifacial modules, higher voltage, improved energy yield), a further 30% solar electricity cost reduction is expected within the next decade, leading power purchase agreements to routinely reach US$ cts 1.3-3 /kWh in most areas in the world. This estimate is based on a reduction of module and inverter costs of 30%, and a reduction of area-related costs by 30% (10% linked to the learning curve, and 20% to efficiency increases and an energy yield increase by 9% attributed to bifaciality and improved temperature coefficient).

To meet the objective of the 2015 Paris agreement and keep the average temperature increase of the Earth below 2 °C, the global emissions of greenhouse gases must be brought down to zero by mid-century. Photovoltaics can play a central role in the transformation of the energy economy. Depending on the scenario, powering the world with sustainable electricity would typically require over 40-70 TW global installed PV capacity [1], [202], [203], which means reaching an annual production volume of 1.5-3 TW per year within the next decade, and then keeping a stabilized production of several TW per year until 2050 [204]. Reaching an annual production target of 2 TW by 2030 would require a 30% annual volume growth from 2020 levels (estimated at 140 GW). Such 30%

annual growth was noteworthily achieved—on average—during the past decade (13 GW in 2011 to 140 GW in 2020). In a less optimistic scenario, an annual growth of 16% would bring the annual production rate to 600 GW per year by 2030, but would require to increase the production of PV modules to a much higher level than in the previous scenario to meet the objectives by 2050; this scenario bears the risk of an overshoot in production capacity after 2050 [204].

In all growth scenarios most of the observed historical trends are expected to continue. For mainstream modules, price pressure will force all stakeholders in the supply chain to reduce their cost, inciting them to minimize the consumption of energy and material, notably by using thinner wafers, less silver, possibly substituted with copper, and less packaging material, while improving module efficiency. Even with conservative estimates for the annual growth in production (16%) and for the price learning curve (18%), a further cost reduction of 30-40% can be expected by 2030 (figure in Box 1). We can expect that the impressive reduction of investment costs (capital expenditure, CAPEX) along the full chain (Fig. 1b) will continue. Noticeably, the CAPEX for a 10 GW (of annual production) PERC solar cell fabrication (from wafer to cells) dropped, in the past 6 years, from around US$ 1.2-1.5 billion to US$ 280 million if sourced in China [202], [205], [206]. At this level, depreciated over 6 years, the impact of CAPEX for a cell line accounts for as little as US$ 0.005 /W. Since higher-efficiency products (interdigitated back contact or SHJ cells) require so far higher CAPEX investments, PV companies targeting fast volume growth have favoured PERC cells in the last years.

Alternative technologies to silicon

With close to 95% of market share in 2020, a well-established supply chain and a standardized design, silicon dominates the PV industry. Although other PV technologies have potential advantages (such as reduced material usage for thin films), taking up large market shares is challenging for them because they have to demonstrate better price and/or efficiency than silicon with at least the same reliability. The thin-film technologies based on copper indium gallium selenide or CdTe have already demonstrated module efficiencies above 19% [10]. Based on the demonstrated cell efficiencies, a similar performance could be expected for perovskites, and a better one in tandem configuration. Other mature technologies, such as thin-film silicon, have been discarded owing to fundamental efficiency limitations (below 15%), and alternative technologies such as polymer or dye sensitised solar cells do not yet have the efficiency level to enter the mainstream market. CdTe PV modules could so far keep up with the drastic price reduction in silicon PV modules. However, the availability of tellurium will most likely become a limitation for multi-TW annual volumes [207]. The best single-junction solar cell efficiency for un-concentrated light is currently obtained with thin GaAs devices with a record value of 29.1% (www.businesswire.com/news/home/20181212005060/en/Alta-Devices-Sets-29.1-Solar-Efficiency-Record). Estimated production costs are, however, more than 100 times higher than for a traditional silicon PV module, forcing the recent stop of the only pilot module manufacturing line [208]. Any new single-junction technology trying to enter the market within the next 5-10 years will be restricted to niche markets (high power density, lightweight, building cladding, automotive). Yet, for c-Si mass production, a solar cell efficiency of 26% is considered by many as a practical limit. An open question thus is what could come next in terms of efficiency.

Today, the only proven concept to further increase efficiency is the combination of solar cells in a multi-junction configuration. Using silicon as a bottom cell, 4-terminal tandem devices have shown

up to 32.8% efficiency (GaAs on Si) and 4-terminal triple junction devices reached 35.9% efficiency (GaIn/GaAs on Si) [209]. Monolithic wafer-bonded triple junctions reached 33.3% efficiency [210], whereas direct epitaxy of III-V on silicon led so far to efficiencies over 25% [211], [212]. Yet, the high cost of growing high-quality III-V thin films will (at best) restrict such devices to niche markets for several years [209].

Currently, the most promising route for high-efficiency and low-cost photovoltaics is the monolithic integration of a perovskite top cell on a silicon bottom cell. In 2018, the first tandem devices with efficiency over 25% were reported [213]–[216]. A couple of devices surpass 29% efficiency [217], [218], and the best certified 4 cm^2 device surpasses 26% [219], all of them using a SHJ bottom cell. The module-level efficiency potential for such devices is over 30%, and even higher with triple-junction configurations, which allows for higher module cost when considering the full PV system [220]. A swift industry adoption could happen through an upgrade of existing Si module production lines with the tools needed for a perovskite top cell, similar to the extraordinarily fast evolution from Al-BSF to PERC cell production. The major challenge will be the demonstration of reliable products, as perovskite devices are particularly sensitive to intrinsic and extrinsic degradation mechanisms, including by contact with air moisture, by exposure to UV light and high temperature, or by electrical biasing. Eventually, the combination of high-bandgap and low-bandgap thin-film solar cells (such as perovskite/perovskite) could combine a high efficiency and a low cost, spelling the death of crystalline silicon PV technology. Nevertheless, beyond competition, synergetic progress of all PV technologies is welcome to meet the objective of 100% renewable energy by 2050.

Conclusions

Silicon photovoltaics has moved at an impressively fast pace to reduce cost, with steady efficiency gains at the cell and module level for commercial products. Many advanced R&D efforts are still ongoing to further improve silicon material and decrease its cost, as well as to improve cell manufacturing, through sharpening current industry-standard processes or developing low-cost approaches and hardware for the realisation of next-generation products incorporating passivating contacts. Combined with the improvements in module technology (larger-area, half-cells, tiling ribbons, shingled cells, multi-wires, back-contacted approaches), this will ensure a further reduction of the efficiency gap between today's record laboratory c-Si solar cells and mainstream modules.

With crystalline silicon occupying a large part of the market and continuously improving, it will be challenging for other technologies to gain or maintain a large market share. Except for niche applications (which still constitute a lot of opportunities), the status of crystalline silicon shows that a solar technology needs to go over 22% module efficiency at a cost below US$ 0.2 /W within the next 5 years to be competitive on the mass market. Higher-efficiency approaches, which command a price premium because of area-related system costs, could be obtained by combining silicon with higher-bandgap top cells, with perovskite being the main candidate for absorber.

Silicon PV devices can be made, even at the TW scale, without any rare or scarce materials, and substitution materials can be used for critical elements (for example silver has been replaced with copper and indium with zinc and/or tin in SHJ). At the unbeatable electricity price level discussed here, there is room for managing solar electricity (long-distance transport, demand-side management, electrochemical storage) and for its transformation into heat, cold or chemicals, such as through power-to-gas processes (H_2, NH_3 and so on), in an economically sustainable way. Hence,

there is no technological limitation to provide the amount of electricity and energy the world needs to make the necessary transition to renewable energy, and political will and economic levers are currently the main roadblocks. The silicon PV industry has gone, in the past three decades, from a curiosity in the energy sector to being “the new king of electricity” as stated by the International Energy Agency (https://www.iea.org/reports/world-energy-outlook-2020). Photovoltaics will play a central role in decarbonising the global energy economy and mitigating climate change, and silicon technology will remain a key player for the next several decades.

Acknowledgements

We thank Dr. Sebastian Joos and Mario Lehman for the design of Fig. 4 and the figure in Box 2, respectively. C. Ballif, M. Boccard, and F.-J. Haug thankfully acknowledge funding by the Horizon 2020 program of the European Union within the projects Ampere under grant 745601 and Highlight under grant 857793, and by the Swiss Federal Office for Energy within the project CHESS under grant SI501253-01, G. Hahn thankfully acknowledges support from the German Federal Ministry of Economic Affairs and Energy.

Table 1: Highest certified efficiencies of various approaches. * denotes a non-certified result. After the area, (da) refers to designated area and (ta) to total area, as discussed in Ref. [75]. For the different cell designs see Fig. 3. Note that several higher-voltage devices were reported by multiple companies as 'PERC' structures without clear description. These devices actually include advanced contacting strategies and they were thus disregarded for inclusion in this table as PERC. V_{OC}: open-circuit voltage; j_{SC}: short-circuit current density; FF: fill factor; Cz: Czochralski; a-Si: amorphous Si; TOPCon: tunnel oxide passivating contact; PERL: passivated emitter, rear locally diffused; PERC: passivated emitter and rear cell; iTOPCon: industrial TOPCon; IBCs: interdigitated back contacts.

Efficiency (%)	Area (cm^2)	V_{oc} (mV)	j_{sc} (mA/cm^2)	FF (%)	Comment	Ref.
Passivating contacts for both polarities in IBCs						
26.7	79.0 (da)	738	42.65	84.9	n-type, heterojunction IBCs	[75], [80]
26.1	4.0 (da)	726.6	42.62	84.3	p-type, tunnel oxide IBCs	[79]
25.0	25.0 (da)	736	41.5	81.9	Tunnel IBC with screen-printing, no lithography	[221]
25.2	153.5 (ta)	737	41.33	82.7	Exact type of contact not disclosed	[222]
25.04	243.2 (ta)	715.6	42.27	82.81	n-type Cz, screen-printed, tunnel-oxide electron contact	[84]
Passivating contacts on both sides						
26.30	274.3	750.2	40.49	86.59	n-type, a-Si heterojunction, M6 wafer, 9 bus bars	[223]
25.1	151 (da)	737.5	40.79	83.5	n-type, a-Si heterojunction, large area, plated	[224]
25.26	244.5 (ta)	748.5	39.48	85.46	n-type, a-Si heterojunction, large area, screen-printed	[100]
22.6*	4.0 (da)	719.6	38.8	80.9	p-type, tunnel oxide with co-annealed poly contacts, screen-printed	[112]
Passivating rear contact, 'classic' metal front contact						
26.0	4.0 (da)	732	42.05	82.3	p-type wafer, n-type TOPCon rear-emitter	[96]
25.8	4.0 (da)	724.1	42.87	83.1	n-type, front by lithography and plating, n-type TOPCon rear-contact	[225], [226]
25.21	243 (ta)	721.6	41.63	83.9	n-type TOPCon, bifacial, screen-printed	[100]
Contacted at the front and rear, with 'classic' metal contacts (PERL or PERC design)						
25.0	4.0 (da)	706.0	42.7	82.2	p-type, metal point contact with local diffusion, original PERL, photolithography, plating	[77]
24.03	244.6 (ta)	694.0	41.6	83.26	Exact structure not disclosed	[227]
23.56	261.4 (ta)	693.2	41.1	82.63	p-type, full wafer area, screen-printed industrial PERC cell, no selective emitter	[227]
Wafers grown from ingot casting (Cast-mono)						
24.4	267.5 (ta)	713.2	41.47	82.5	n-type, iTOPCon	[75]
22.8	246.7 (ta)	687.1	40.90	81.2	p-type, highest monocrystalline cell efficiency in "mass production", screen-printed	[75]

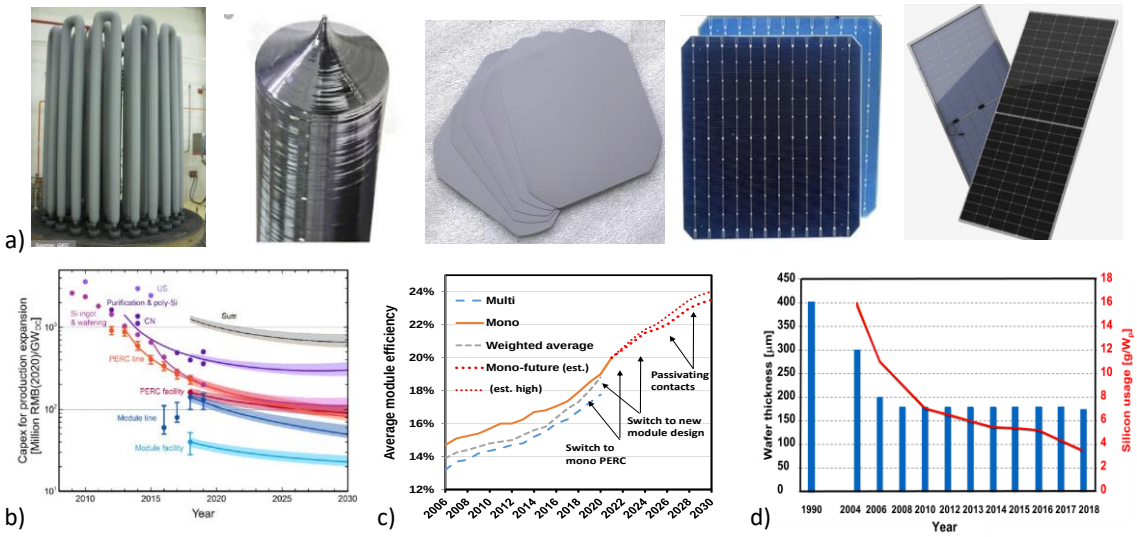

Fig. 1: From raw silicon to solar modules. a) The main steps in making photovoltaic (PV) modules: purified polysilicon preparation [230], crystalline ingot casting or pulling, wafering, solar cell processing and module assembly. b) Learning curve in capital expenditure (Capex) along the value chain, from polysilicon purification to modules assemble. Symbols indicate historical data, lines predicted future trends for passivated emitter and rear cells (PERC). c) Average efficiency evolution of monocrystalline and multi-crystalline silicon mainstream modules, considering all modules sold on the market. An estimate for future improvements in the efficiency of monocrystalline cells is provided. d) Decrease in wafer thickness and silicon consumption over time. Panel b adapted from Ref. [231]. Panels c and d adapted from Ref. [232].

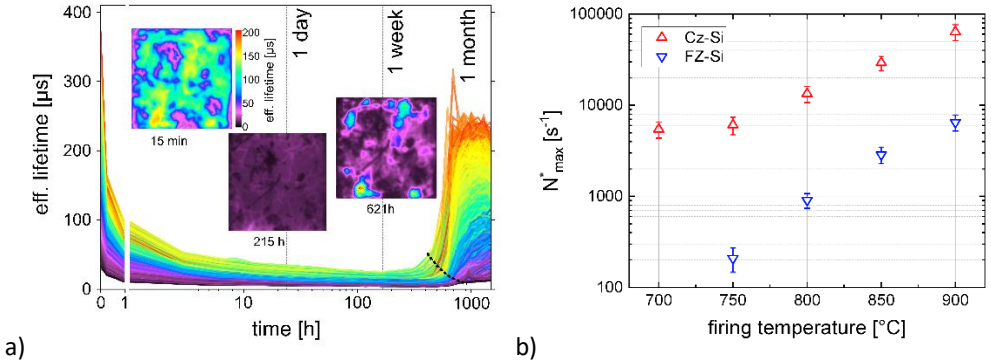

Fig. 2: Defect creation in silicon as a function of light and temperature. a) Spatially resolved effective charge carrier lifetime, τ_{eff}, of a p-type 5x5 cm^2 multi-crystalline Si sample under 75 °C and 1 sun illumination measured using time-resolved photoluminescence imaging *[38]*. Each line represents the τ_{eff} of a 100 x 100 µm^2 sample area, with the color code scaled to the value before illumination. All wafer areas show a severe light- and elevated-temperature-induced degradation (LeTID) effect, with areas of higher initial material quality regenerating earlier than poor-quality areas (dashed line). Inset: lifetime maps at different points in time. At maximum degradation (around 215 h), areas near grain boundaries show longer lifetimes than the neighbouring grains. The first hour is shown on a linear scale, the rest on a logarithmic scale. The SiN_x:H surface passivation layer was deposited by plasma-enhanced chemical vapour deposition and fired at 800 °C peak sample temperature. b) Maximum equivalent defect concentration N^*_{max} during a degradation experiment using boron-doped Czochralski (Cz) and float-zone (FZ) Si wafers coated with SiN_x:H [233]. Higher firing temperatures lead to increased N^*_{max}, possibly owing to increased concentrations of hydrogen in the silicon bulk. Note that for Cz-Si both phenomena, LeTID and boron-oxygen-related light-induced degradation, are present, resulting in a higher N^*_{max} compared to FZ-Si. Panel a adapted from Ref. [38], panel b from Ref. [233].

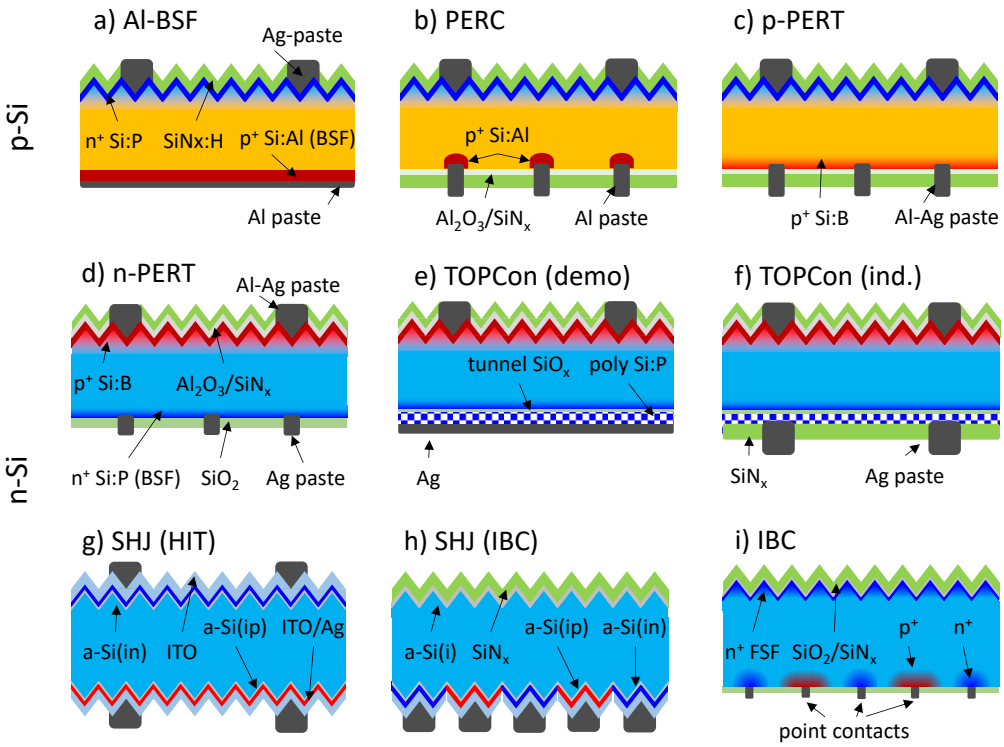

Fig. 3: Schematic representation of typical solar cell architectures. a) A simple cell design based on p-type Si with phosphorous diffusion forming a highly n^+-doped front and full-area Al rear contact forming a highly p^+-doped rear; this type of cell is called Al back surface field (Al-BSF). b) Localised rear contacts in the passivated emitter and rear cell (PERC) architecture. c,d) Local contacts are also used in passivated emitter and rear totally diffused (PERT) cells a design that applies to p-type (panel c) as well as n-type (panel d) wafers. e,f) n-type cells with a tunnel oxide passivating contact (TOPCon) design, either with evaporated Ag contact as used in R&D (panel e), or with localised fire-through metallisation as introduced in industry (panel f). g) A rear-contacted silicon heterojunction (SHJ) using IBC. h) A SHJ design, also called heterojunction with intrinsic thin layer (HIT), contacted on both sides with intrinsic and doped bilayers (in and ip at front and rear, respectively) and indium tin oxide (ITO). i) Interdigitated back contacts (IBC) design with n^+-doped front surface field (FSF).

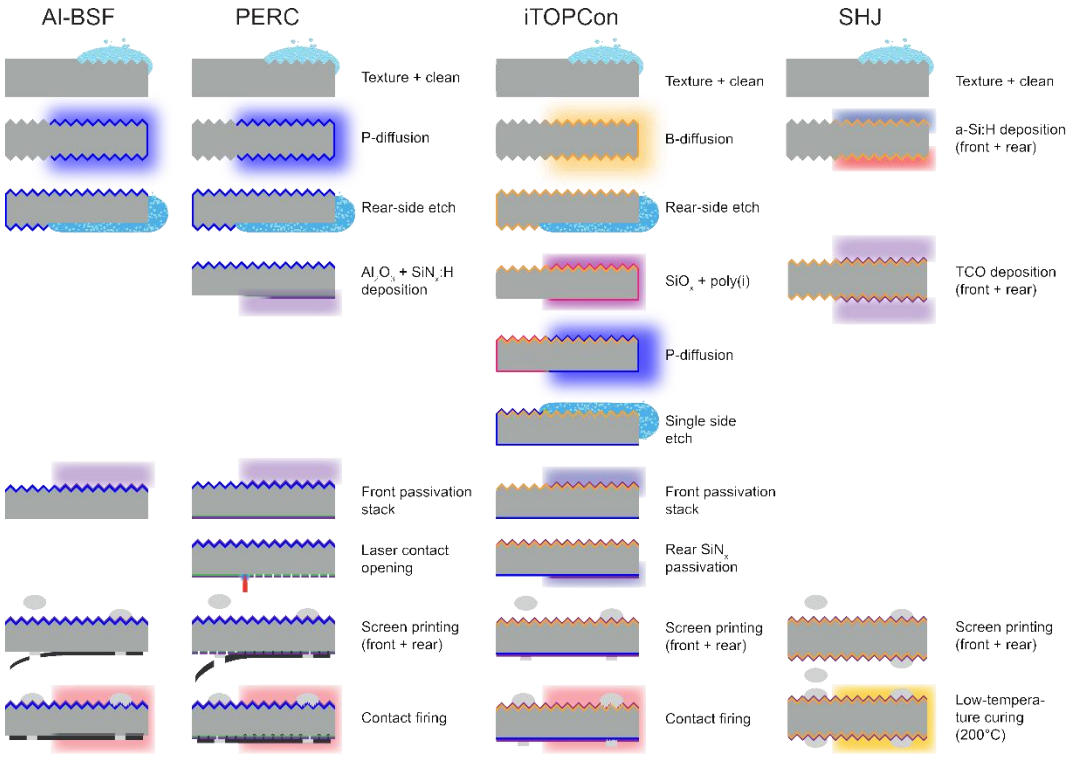

Fig. 4: Schematic process flows for the fabrication of solar cells using different architectures. In most passivated emitter and rear cell (PERC) cells a 'selective' emitter is created by adding a third step after the phosphorus diffusion, in which the phosphorus glass and crystalline-Si surface are molten by a laser to create a highly doped region in the areas where the metallisation fingers are printed later. Note that despite the simplicity of the silicon heterojunction (SHJ) process flow, production of SHJ cells is currently costlier than that of PERC cells owing to the use of more expensive equipment, higher material costs, and a lower line throughput. BSF: back surface field; iTOPCon: industrial tunnel oxide passivating contact. Figure adapted from Ref. [234].

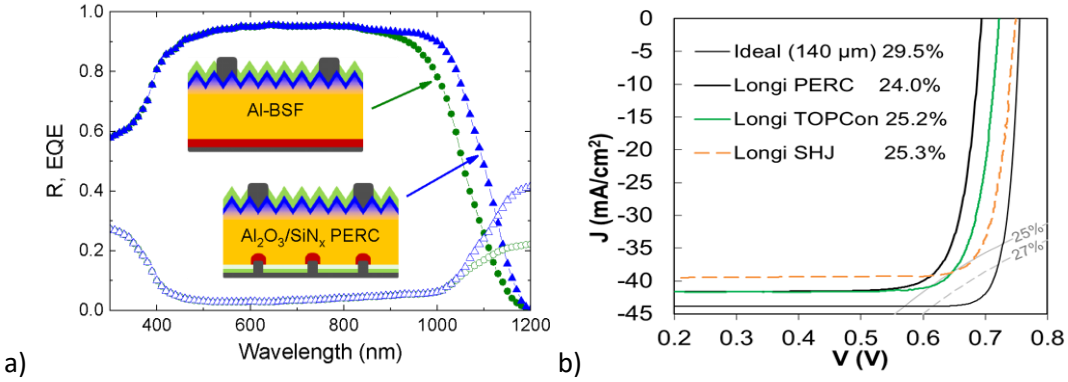

Fig. 5. Typical performance characteristics of c-Si solar cells. a) External quantum efficiency (full symbols) and reflection (open symbols) for an Al-doped back surface field (Al-BSF, circles) and a passivated emitter and rear cell (PERC) solar cell (triangles). b) Current-voltage curves for a PERC cell, a cell with a tunnel oxide passivating contact (TOPCon) and silicon heterojunction (SHJ) cell compared to the theoretical limit [75], [218]. Panel a adapted from Ref. [235].

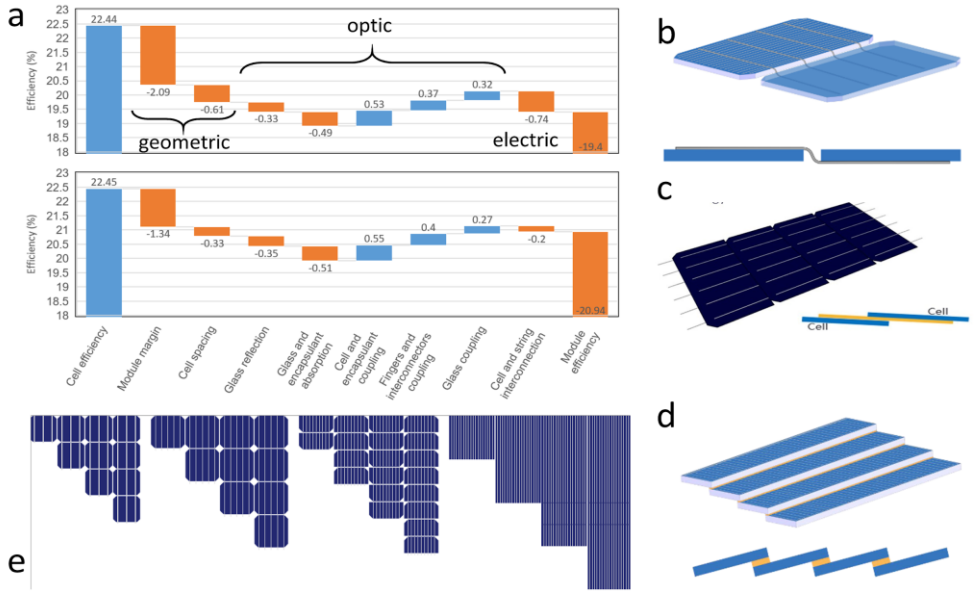

Fig. 6. From cells to modules. a) Typical cell-to-module loss analysis performed with the modelling package SmartCalc.CTM (www.cell-to-module.com) for a 2017 premium module scheme of 1.7 m^2 consisting of 60 156-mm pseudo-square wafers connected with five busbars (top), as in the top sketch in panel c, and for a 2021 module of 2.4 m^2 consisting of 150 third-cut 210-mm full-square wafers connected with nine busbars (bottom) with tiling of the cells, as in the middle sketch in panel c. The main improvements lay in the area coverage (two first elements) and in the interconnection (last one). b) Evolution of standard module design from the years 2000 to 2021. The first sketch represents 125-mm quasi-square wafers using three busbars and standard interconnection (as in panel c, top). The second sketch shows 156-mm quasi-square wafers with five busbars, which was standard in 2017, corresponding to the first cell-to-module analysis shown in panel a. The third sketch shows 156.75-mm half-cut quasi-square wafers with nine busbars, which is illustrative of the 2016-2020 evolution. The last sketch represents one of many 2021's options with 210-mm third-cut full-square wafers using tiling ribbon interconnections (as in panel c, middle). Quasi-square wafers prevent material waste when cutting a square from a cylindrical ingot: 150-mm-diameter ingots were typically used for 125-mm-wide wafers, moving to 200-mm and 210-mm diameters for wafers 156-mm and 156.75-mm wide, respectively. The latter size enables wafers with a lower fraction of lost area in the missing corners, but a larger share of the ingot discarded. **c)** Sketches of the interconnection for the two modules compared in panel a, using standard interconnections (top) and a tiling ribbon design (middle), and of the interconnection for shingled modules (bottom). Panel c (top and bottom) adapted from http://www.metallizationworkshop.info/fileadmin/layout/images/Konstanz-2017/MWS2017/VIII_4_Klasen.pdf, panel c (middle) from https://www.solarpowerpanels.net.au/longi-shows-off-its-new-shingled-seamless-soldered-module/

Box 1: A historical perspective

The US Bell Laboratories demonstrated the first solar cell of practical interest, with 6% efficiency, in 1954 [236]. In the following years, the main market driver for silicon cells was space applications, whereas the terrestrial market was limited mostly to off-grid applications. The small manufacturing volumes translated into high prices, preventing any massive deployment of photovoltaics. The first terrestrial photovoltaic (PV) power plant, of 1 MW in capacity, was built in 1982.

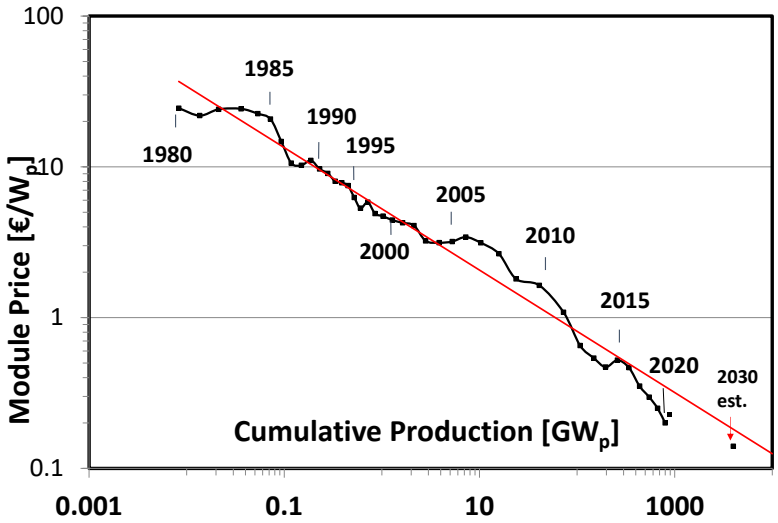

In the years from 1980 to early 1990, the most important technological bricks for the realisation of high-performance and/or industrial silicon solar cells were developed, building on microelectronics and power semiconductor technologies. Monocrystalline solar cells reached efficiencies of 20% in the laboratory in 1985 [237], and of 26.2% under 100x concentration in 1988 [238]. In this period, the efficiency of industrial solar cells slowly grew from 12% to 14.5%. The challenge was still to find a way to go from, for example, US$ 4-5 /W in 1994 [239] down by a factor at least 10 to make photovoltaics a competitive electricity source, a goal that required technology improvements, larger production volume and a dedicated supply chain. Globally, many countries provided significant contributions to the PV industry in the past 50 years: first the USA with its large PV market for satellites and the first large-scale PV plants, then Australia with its large remote PV-powered telecommunication market and Japan with the first significant residential PV market. A large acceleration took place at the beginning of the 21st century, with innovative and significant feed-in tariffs in Germany and many European countries [240], which triggered a vast effort of EU equipment makers, enabling enhanced manufacturing capability for the industry. Finally, China played a major role in manufacturing, through large financial support from international investors, particularly from the US, which supported low-cost mass industrialization.

The incentive schemes triggered, from 2000 to 2010, a strong market growth of over 30% per year, and had profound effects. For the first time in 2004, the PV industry used more silicon (in weight) than the entire semiconductor industry, leading to a shortage of refined polysilicon from 2004 to 2009. The price of solar-grade polysilicon feedstock reached US$ 400 /kg, up from US$ 30-50 /kg before the shortage. This triggered investment in large polysilicon production plants, enabling prices as low as US$ 6-12 /kg in 2021. In parallel, the production capacity increased for solar cells and solar modules, mainly in Asia and in particular in China, leading to global overinvestment and oversupply.

The selling price of modules dropped fast in 2010-2015, forcing many companies out of business. The mass industrialisation proceeded with a volume growth of around 25% per year over the past decade, exceeding 130 GW in 2020. This corresponds to an area of 630 km^2 of crystalline (c-)Si modules, representing over 95% of the PV market [10]. From 1980 to 2020, PV module prices decreased by 24% for each doubling of the cumulated produced capacity, as shown on the figure. Assuming constant margins, this suggests a learning rate of 24% over the past four decades also in terms of cost. A learning rate of 40% can be observed for the past decade, explained by the recovery from the early 2000s shortage followed by the concentration of a manufacturing cluster in China, and standardization of tools, processes and designs throughout the entire supply chain. Today's typical wholesale price for mainstream c-Si modules is in the range of US$ 0.17-0.25 /W [10] depending on the type and efficiency, which converts to a staggering low US$ 35-50 /m^2.

Data until 2020 adapted from Ref. [71] (Fischer et al.)

Box 2: The different kinds of silicon

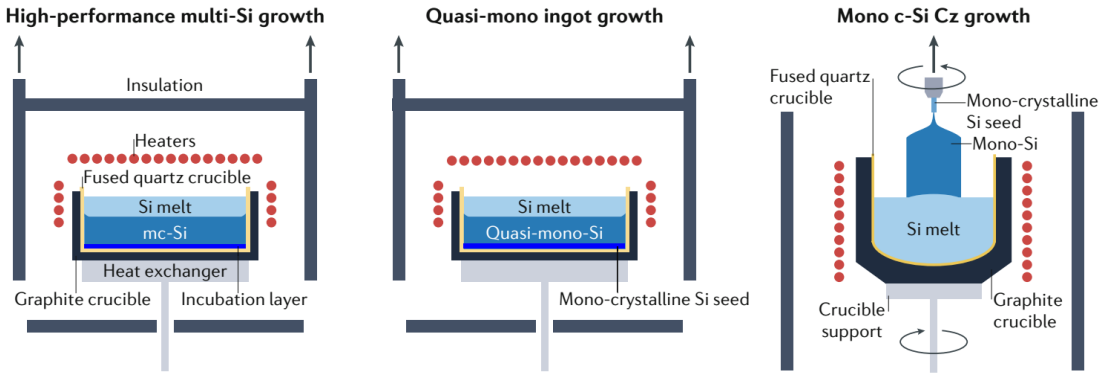

Silicon wafers used for photovoltaics can be distinguished by the way they have been crystallized. Over the past two decades multi-crystalline silicon (mc-Si) wafers made by directional solidification (DS) have represented on average about 60% of the market. In DS, the molten silicon is slowly crystallized from bottom to top in a square-shaped crucible made of fused silica coated with silicon nitride (SiN_x, left panel of the figure). Every solidification requires a new crucible. The bottom of the crucible contains seeds to influence the crystal growth [241], [242], [38]. This 'incubation layer', made of small pieces of silicon, silicon dioxide, silicon nitride, silicon carbide, or other high-temperature materials, is used as a seed to obtain relatively small grains of typically a few millimetres that relax crystallographic dislocations more easily than large grains. This type of Si is referred to as high-performance multi-crystalline ('HP-multi') material. Alternatively, the use of monocrystalline seeds results in large parts of the ingot having a monocrystalline structure ('quasi-mono' or 'cast-mono' material, middle part of the figure) [243]. The size of the crucibles is continuously increasing: ingots of up to 1,650 kg can be solidified.

Driven by the development of high-efficiency passivated emitter and rear cell (PERC) solar cells, that require substrates of better quality, and recent improvement in the Czochralski (Cz) process, that enables multiple recharge and multiple-ingot pulling, the year 2018 has seen a significant change in the silicon wafer market. The major share of the current market is now based on monocrystalline ingots grown via the Cz method (right panel of the figure). Here, a seed crystal is dipped into molten silicon contained in a rotating quartz crucible and slowly pulled upwards, resulting in a ~2 m long cylindrically shaped single crystal of typically 200-300 mm in diameter. The crucible can be recharged while still hot, and three to five ingots can be pulled without cooling and breaking the controlled atmosphere [244]–[246]. Eventually, detrimental metal impurities accumulate in the melt owing to their higher solubility in the liquid phase, and the crucible with the residual melt must be changed. The fracture strength of the seed crystal, with its typical diameter of 3 mm, limits the maximum ingot weight and thus its length.

The DS process yields Si ingots at a lower cost than the Cz method thanks to a higher throughput and lower energy consumption. DS silicon is, however, so far more defective than Cz silicon due to impurity diffusion from the crucible, but also precipitates, dislocations, and grain boundaries that depend on the position in the ingot and on external parameters such as the cooling rate. However, the quality of silicon can be significantly improved during cell fabrication. As an indication, the world record solar cell efficiencies for DS ingots are 22.8% for multi-crystalline Si and 24.4% for quasi-mono Si [75]. Conversely, the main impurities in Cz Ingots are oxygen and carbon, which can reach concentrations up to 10^{18} cm^{-3} and $5x10^{16}$ cm^{-3}, respectively [247]; lower concentrations are possible by a careful design of the puller [7]. The float-zone crystal growth technique, often

used to reach high performances in laboratories, is currently not used in the photovoltaic industry owing to cost considerations and material-quality improvements of Cz silicon.

Several wafering technologies that avoid the ingot sawing step are under development. In direct epitaxy [248], a monocrystalline silicon substrate is treated to form a porous silicon layer. Following a heat treatment, epitaxial silicon is deposited to the desired thickness using silane or chlorosilanes. Afterwards, the grown layer can be lifted off [249]. For ribbon silicon [250], a thin sheet of multi-crystalline silicon is pulled from the melt and cut into wafers. The Direct Wafer® technology [251] grows multi-crystalline wafers from the melt by selectively cooling the surface and lifting off the solidified sheet.

Figure courtesy of Mario Lehman.

Box 3: Key losses in a silicon solar cell

A perfect solar cell would have no losses apart from the ones dictated by physics or thermodynamics. In a semiconductor, photons with energy lower than the bandgap are not absorbed. For absorbed photons, the part of their energy exceeding the bandgap is dissipated into heat in a process called thermalisation. The theoretical efficiency limit of a solar cell is then governed by radiative recombination, which is the reciprocal process of absorption. For a semiconductor with a bandgap of 1.1 eV, this process yields a limiting efficiency of 32% [252], [253]. For crystalline silicon, the limiting recombination process is not radiative recombination, but Auger recombination, which is independent of how pure and perfect the substrate is. To assess the maximum theoretical efficiency, it is therefore mandatory to accurately determine the parameters of the Auger process. Several models have been proposed [254]–[256], placing the efficiency limit around 29.5% [254], [255], [257]. In addition to these fundamental loss mechanisms, other practical losses limit the efficiency of real solar cells. These include recombination at defects, optical losses and resistive losses.

Recombination losses in the bulk are assessed by measuring the bulk lifetime τ_{bulk} of excess charge carriers. The crystal surfaces at the front and rear contribute additional recombination losses that are generally expressed by the surface recombination velocities S_f and S_r. A thermal oxidation of the surface is an excellent way to reduce the carrier recombination at the interface. For many years, this process step had been considered too expensive to be used in industrial manufacturing of low-cost solar cells. It has, however, been recently introduced in large-volume manufacturing before silicon nitride (SiN_x:H) deposition. Traditionally, the low-cost method to reduce the carrier recombination at the interfaces was to introduce a high-low doping profile that reduces the minority-carrier density at the interface, for example in the back surface field. Field-induced accumulation or inversion layers have the same effect of reducing the effective surface recombination. Current high-efficiency silicon solar cells combine a thin silicon oxide layer with positive charges with a layer of SiN_x:H for n-type Si, or with negative charges with a layer of Al_2O_3 for p-type Si.

All recombination pathways add up in parallel, leading to the definition of an effective carrier lifetime τ_{eff}, which in the case of a uniform carrier concentration across a device with reasonably good surface passivation can be written as:

$$\frac{1}{\tau_{eff}} = \frac{1}{\tau_{bulk}} + \frac{1}{\tau_{surface}} = \sum_i \frac{1}{\tau_{bulk,i}} + \frac{S_f}{W} + \frac{S_r}{W}$$

where τ_{bulk}contains contributions of radiative recombination, Auger processes and trap-associated carrier lifetimes, whereas $\tau_{surface}$ is defined in terms of S_f and S_r and the device thickness W. A high value of τ_{eff} assures low recombination rates of the generated excess charge carriers and thus enables building up a high internal voltage.

Optical losses occur by shading of the metal contacts (~3-4%), surface reflection (~3%), parasitic absorption in dielectric layers and contacts (<1%), free-carrier absorption (<1%) or imperfect light management (<1%). A good light-trapping scheme, combining anti-reflection coating, surface texture, good internal surface reflectivity, highly reflective metals for IR wavelengths and low doping to avoid free-carrier absorption, should be applied to significantly increase the path length of weakly absorbed long-wavelength photons and to guarantee that they can be absorbed in the silicon crystal. In addition, sub-bandgap photons of wavelengths greater than 1200 nm should ideally be reflected to avoid unnecessary heating of the solar cell.

Series resistance can be another significant source of power loss, in particular in the emitter, the metal fingers and the interconnection. These losses are mitigated through continuous technology improvements, such as decreasing finger pitch (while decreasing finger width to maintain a low shadowing), multi-busbar or wire interconnection (9 to 20), and cutting cells in half or even in smaller sub-cells.

Related links

SmartCalc.CTM (www.cell-to-module.com)

a record value of 29.1% (www.businesswire.com/news/home/20181212005060/en/Alta-Devices-Sets-29.1-Solar-Efficiency-Record)

as stated by the International Energy Agency (https://www.iea.org/reports/world-energy-outlook-2020)

References

[1] N. M. Haegel *et al.*, "Terawatt-scale photovoltaics: Trajectories and challenges," *Science*, vol. 356, no. 6334, pp. 141–143, Apr. 2017, doi: 10.1126/science.aal1288.

[2] S. K. Chunduri and M. Schmela, "Market survey polysilicon CVD reactors 2017 | TaiyangNews." [Online]. Available: http://taiyangnews.info/reports/market-survey-cvd-reactors/

[3] Y. Wan, S. R. Parthasarathy, C. Chartier, A. Servini, and C. P. Khattak, "Increased polysilicon deposition in a CVD reactor," Jun. 2006

[4] M. Osborne, "GCL-Poly touts FBR silicon matching Siemens process on purity," *PV Tech*, Mar. 09, 2021. https://www.pv-tech.org/gcl-poly-touts-fbr-silicon-matching-siemens-process-on-purity/ (accessed Oct. 06, 2021).

[5] G. Bye and B. Ceccaroli, "Solar grade silicon: Technology status and industrial trends," *Sol. Energy Mater. Sol. Cells*, vol. 130, pp. 634–646, 2014.

[6] J. Czochralski, "A new method for the measurement of the crystallization rate of metals," *Z. Für Phys. Chem.-Stochiometrie Verwandtschaftslehre*, vol. 92, no. 2, pp. 219–221, 1917.

[7] W. Zulehner, "Czochralski growth of silicon," *J. Cryst. Growth*, vol. 65, no. 1, pp. 189–213, 1983, doi: https://doi.org/10.1016/0022-0248(83)90051-9.

[8] H. J. Möller, "Wafering of silicon crystals," in *Physica Status Solidi (A) Applications and Materials Science*, Mar. 2006, vol. 203, no. 4, pp. 659–669. doi: 10.1002/pssa.200564508.

[9] T. Enomoto, Y. Shimazaki, Y. Tani, M. Suzuki, and Y. Kanda, "Development of a resinoid diamond wire containing metal powder for slicing a slicing ingot," *CIRP Ann.*, vol. 48, no. 1, pp. 273–276, 1999, doi: 10.1016/S0007-8506(07)63182-5.

[10] S. Philipps and W. Warmuth, "Fraunhofer ISE: Photovoltaics Report, updated: 27 July 2021," 2021. [Online]. Available: https://www.ise.fraunhofer.de/en/publications/studies/photovoltaics-report.html

[11] V. Fthenakis and M. Raugei, "Environmental life-cycle assessment of photovoltaic systems," in *The Performance of Photovoltaic (PV) Systems*, Elsevier, 2017, pp. 209–232.

[12] A. G. Aberle, "Surface passivation of crystalline silicon solar cells: a review," *Prog. Photovolt. Res. Appl.*, vol. 8, no. 5, pp. 473–487, 2000.

[13] S. Dauwe, L. Mittelstädt, A. Metz, and R. Hezel, "Experimental evidence of parasitic shunting in silicon nitride rear surface passivated solar cells," *Prog. Photovolt. Res. Appl.*, vol. 10, no. 4, pp. 271–278, 2002.

[14] R. S. Bonilla, I. Al-Dhahir, M. Yu, P. Hamer, and P. P. Altermatt, "Charge fluctuations at the Si–SiO2 interface and its effect on surface recombination in solar cells," *Sol. Energy Mater. Sol. Cells*, vol. 215, pp. 110649–110649, 2020.

[15] T. Buonassisi *et al.*, “Chemical natures and distributions of metal impurities in multicrystalline silicon materials,” *Prog. Photovolt. Res. Appl.*, vol. 14, no. 6, pp. 513–531, Sep. 2006, doi: 10.1002/pip.690.
[16] M. Seibt and V. Kveder, “Gettering Processes and the Role of Extended Defects,” in *Advanced Silicon Materials for Photovoltaic Applications*, 2012, pp. 127–188. doi: 10.1002/9781118312193.ch4.
[17] A. Ourmazd and W. Schröter, “Phosphorus gettering and intrinsic gettering of nickel in silicon,” *Appl. Phys. Lett.*, vol. 45, no. 7, pp. 781–783, Oct. 1984, doi: 10.1063/1.95364.
[18] A. Y. Liu, C. Sun, V. P. Markevich, A. R. Peaker, J. D. Murphy, and D. Macdonald, “Gettering of interstitial iron in silicon by plasma-enhanced chemical vapour deposited silicon nitride films,” *J. Appl. Phys.*, vol. 120, no. 19, pp. 193103–193103, Nov. 2016, doi: 10.1063/1.4967914.
[19] S. Gindner, P. Karzel, B. Herzog, and G. Hahn, “Efficacy of phosphorus gettering and hydrogenation in multicrystalline silicon,” *IEEE J. Photovolt.*, vol. 4, no. 4, pp. 1063–1070, Jul. 2014, doi: 10.1109/JPHOTOV.2014.2322276.
[20] P. Karzel *et al.*, “Dependence of phosphorus gettering and hydrogen passivation efficacy on grain boundary type in multicrystalline silicon,” *J. Appl. Phys.*, vol. 114, no. 24, pp. 244902–244902, Dec. 2013, doi: 10.1063/1.4856215.
[21] H. C. Sio and D. Macdonald, “Direct comparison of the electrical properties of multicrystalline silicon materials for solar cells: Conventional p-type, n-type and high performance p-type,” *Sol. Energy Mater. Sol. Cells*, 2016, doi: 10.1016/j.solmat.2015.09.011.
[22] S. P. Phang *et al.*, “N-type high-performance multicrystalline and mono-like silicon wafers with lifetimes above 2 ms,” *Jpn. J. Appl. Phys.*, vol. 56, no. 8S2, pp. 08MB10-08MB10, Aug. 2017, doi: 10.7567/JJAP.56.08MB10.
[23] H. Fischer and W. Pschunder, “Investigations on photon and thermal induced changes in silicon solar cells,” in *Proceedings of the 10th IEEE Photovoltaic Specialists Conference, Palo Alto*, 1973, pp. 404–404.
[24] S. W. Glunz, S. Rein, W. Warta, J. Knobloch, and W. Wettling, “Degradation of carrier lifetime in Cz silicon solar cells,” *Sol. Energy Mater. Sol. Cells*, 2001, doi: 10.1016/S0927-0248(00)00098-2.
[25] S. Rein, S. Diez, R. Flaster, and S. W. Glunz, “Quantitative correlation of the metastable defect in Cz-silicon with different impurities,” *3rd World Conf. Photovolt. Energy Convers.*, pp. 1048–1052, 2003.
[26] K. Bothe, R. Sinton, and J. Schmidt, “Fundamental boron-oxygen-related carrier lifetime limit in mono- And multicrystalline silicon,” *Prog. Photovolt. Res. Appl.*, vol. 13, no. 4, pp. 287–296, 2005, doi: 10.1002/pip.586.
[27] A. Herguth, G. Schubert, M. Kaes, and G. Hahn, “A new approach to prevent the negative impact of the metastable defect in boron doped CZ silicon solar cells,” in *Conference Record of the 2006 IEEE 4th World Conference on Photovoltaic Energy Conversion, WCPEC-4*, 2007, vol. 1, pp. 940–943. doi: 10.1109/WCPEC.2006.279611.
[28] S. Wilking, A. Herguth, and G. Hahn, “Influence of hydrogen on the regeneration of boron-oxygen related defects in crystalline silicon,” *J. Appl. Phys.*, vol. 113, no. 19, May 2013, doi: 10.1063/1.4804310.
[29] A. Herguth and G. Hahn, “Kinetics of the boron-oxygen related defect in theory and experiment,” *J. Appl. Phys.*, vol. 108, no. 11, Dec. 2010, doi: 10.1063/1.3517155.
[30] A. Herguth and B. Hallam, “A generalized model for boron-oxygen related light-induced degradation in crystalline silicon,” in *AIP Conference Proceedings*, Aug. 2018, vol. 1999. doi: 10.1063/1.5049325.
[31] B. J. Hallam, M. D. Abbott, N. Nampalli, P. G. Hamer, and S. R. Wenham, “Implications of accelerated recombination-active defect complex formation for mitigating carrier-induced degradation in silicon,” *IEEE J. Photovolt.*, vol. 6, no. 1, pp. 92–99, Jan. 2016, doi: 10.1109/JPHOTOV.2015.2494691.

[32] C. Derricks, A. Herguth, G. Hahn, O. Romer, and T. Pernau, “Industrially applicable mitigation of BO-LID in Cz-Si PERC-type solar cells within a coupled fast firing and halogen lamp based belt-line regenerator – A parameter study,” *Sol. Energy Mater. Sol. Cells*, vol. 195, pp. 358–366, Jun. 2019, doi: 10.1016/j.solmat.2019.03.020.

[33] A. Herguth and G. Hahn, “Towards a high throughput solution for boron-oxygen related regeneration,” in *28th European Photovoltaic Solar Energy Conference and Exhibition*, 2013, pp. 1507–1511.

[34] J. Ye, B. Ai, J. Jin, D. Qiu, R. Liang, and H. Shen, “Study on the Electrical Injection Regeneration of Industrialized B-Doped Czochralski Silicon PERC Solar Cells,” *Int. J. Photoenergy*, vol. 2019, 2019.

[35] “International Technology Roadmap for Photovoltaics (ITRPV).” [Online]. Available: www.itrp.net

[36] K. Ramspeck *et al.*, “Light induced degradation of rear passivated mc-Si solar cells,” in *Proc. 27th Eur. Photovolt. Sol. Energy Conf. Exhib.*, 2012, vol. 1, pp. 861–865.

[37] F. Kersten *et al.*, “Degradation of multicrystalline silicon solar cells and modules after illumination at elevated temperature,” *Sol. Energy Mater. Sol. Cells*, vol. 142, pp. 83–86, Nov. 2015, doi: 10.1016/j.solmat.2015.06.015.

[38] A. Zuschlag, D. Skorka, and G. Hahn, “Degradation and regeneration in mc-Si after different gettering steps,” *Prog. Photovolt. Res. Appl.*, vol. 25, no. 7, pp. 545–552, Jul. 2017, doi: 10.1002/pip.2832.

[39] D. Skorka, A. Zuschlag, and G. Hahn, “Firing and gettering dependence of effective defect density in material exhibiting LeTID,” in *AIP Conference Proceedings*, Aug. 2018, vol. 1999. doi: 10.1063/1.5049334.

[40] D. Sperber, A. Heilemann, A. Herguth, and G. Hahn, “Temperature and light-induced changes in bulk and passivation quality of boron-doped float-zone silicon coated with SiNx:H,” *IEEE J. Photovolt.*, vol. 7, no. 2, pp. 463–470, Mar. 2017, doi: 10.1109/JPHOTOV.2017.2649601.

[41] T. Niewelt, M. Selinger, N. E. Grant, W. Kwapil, J. D. Murphy, and M. C. Schubert, “Light-induced activation and deactivation of bulk defects in boron-doped float-zone silicon,” *J. Appl. Phys.*, vol. 121, no. 18, May 2017, doi: 10.1063/1.4983024.

[42] D. Chen *et al.*, “Hydrogen induced degradation: A possible mechanism for light-and elevated temperature-induced degradation in n-type silicon,” *Sol. Energy Mater. Sol. Cells*, vol. 185, pp. 174–182, 2018.

[43] J. Lindroos, A. Zuschlag, D. Skorka, and G. Hahn, “Silicon Nitride Deposition: Impact on Lifetime and Light-Induced Degradation at Elevated Temperature in Multicrystalline Silicon,” *IEEE J. Photovolt.*, pp. 1–11, 2019, doi: 10.1109/JPHOTOV.2019.2945164.

[44] D. Bredemeier, D. Walter, S. Herlufsen, and J. Schmidt, “Lifetime degradation and regeneration in multicrystalline silicon under illumination at elevated temperature,” *AIP Adv.*, vol. 6, no. 3, Mar. 2016, doi: 10.1063/1.4944839.

[45] T. H. Fung *et al.*, “A four-state kinetic model for the carrier-induced degradation in multicrystalline silicon: Introducing the reservoir state,” *Sol. Energy Mater. Sol. Cells*, vol. 184, pp. 48–56, Sep. 2018, doi: 10.1016/j.solmat.2018.04.024.

[46] C. Sen *et al.*, “Annealing prior to contact firing: A potential new approach to suppress LeTID,” *Sol. Energy Mater. Sol. Cells*, vol. 200, pp. 109938–109938, 2019.

[47] H. Steinkemper, M. Hermle, and S. W. Glunz, “Comprehensive simulation study of industrially relevant silicon solar cell architectures for an optimal material parameter choice,” *Prog. Photovolt. Res. Appl.*, vol. 24, no. 10, pp. 1319–1331, Oct. 2016, doi: 10.1002/pip.2790.

[48] A. Cuevas and D. Yan, “Misconceptions and misnomers in solar cells,” *IEEE J. Photovolt.*, vol. 3, no. 2, pp. 916–923, 2013.

[49] R. J. Falster, M. Cornara, D. Gambaro, M. Olmo, and M. Pagani, “Effect of high temperature pre-anneal on oxygen precipitates nucleation kinetics in Si,” in *Solid state phenomena*, 1997, vol. 57, pp. 123–128.

[50] J. Mandelkorn and J. H. Lamneck Jr, “A new electric field effect in silicon solar cells,” *J. Appl. Phys.*, vol. 44, no. 10, pp. 4785–4787, 1973.
[51] J. Mandelkorn and J. H. Lamneck, “Simplified fabrication of back surface electric field silicon cells and novel characteristics of such cells,” *Sol. Cells*, vol. 29, no. 2, pp. 121–130, Aug. 1990, doi: 10.1016/0379-6787(90)90021-V.
[52] E. L. Ralph, “Recent advancements in low cost solar cell processing,” in *Records of the 11th Photovoltaic Specialists Conference, Scottsdale, AZ, USA*, 1975, pp. 315–316.
[53] M. A. Green, “Enhancement of Schottky solar cell efficiency above its semiempirical limit,” *Appl. Phys. Lett.*, vol. 27, no. 5, pp. 287–288, 1975.
[54] R. M. Swanson, “Point-contact solar cells: modeling and experiment,” *Sol. Cells*, vol. 17, no. 1, pp. 85–118, 1986.
[55] M. A. Green, “The path to 25% silicon solar cell efficiency: History of silicon cell evolution,” *Prog. Photovolt. Res. Appl.*, vol. 17, no. 3, pp. 183–189, May 2009, doi: 10.1002/pip.892.
[56] A. W. Blakers, A. Wang, A. M. Milne, J. Zhao, and M. A. Green, “22.8% efficient silicon solar cell,” *Appl. Phys. Lett.*, vol. 55, no. 13, pp. 1363–1365, 1989.
[57] M. Taguchi *et al.*, “24.7% record efficiency HIT solar cell on thin silicon wafer,” *IEEE J. Photovolt.*, vol. 4, no. 1, pp. 96–99, 2014.
[58] E. Yablonovitch, T. Gmitter, R. M. Swanson, and Y. H. Kwark, “A 720 mV open circuit voltage SiOx:c-Si:SiOx double heterostructure solar cell,” *Appl. Phys. Lett.*, vol. 47, no. 11, pp. 1211–1213, 1985, doi: 10.1063/1.96331.
[59] F. Feldmann, M. Bivour, C. Reichel, H. Steinkemper, M. Hermle, and S. W. Glunz, “Tunnel oxide passivated contacts as an alternative to partial rear contacts,” *Sol. Energy Mater. Sol. Cells*, vol. 131, pp. 46–50, 2014.
[60] W. Wu *et al.*, “Development of industrial n-type bifacial topcon solar cells and modules,” in *Proceedings of the 36th European Photovoltaic Solar Energy Conference and Exhibition*, 2019, pp. 100–102.
[61] T. G. Allen, J. Bullock, X. Yang, A. Javey, and S. De Wolf, “Passivating contacts for crystalline silicon solar cells,” *Nat. Energy*, Sep. 2019, doi: 10.1038/s41560-019-0463-6.
[62] F. Huster and others, “Investigation of the alloying process of screen printed aluminium pastes for the BSF formation on silicon solar cells,” in *Proceedings of the 20th European Photovoltaic Solar Energy Conference*, 2005, pp. 1466–1469.
[63] C. Ballif, D. Huljić, G. Willeke, and A. Hessler-Wyser, “Silver thick-film contacts on highly doped n-type silicon emitters: structural and electronic properties of the interface,” *Appl. Phys. Lett.*, vol. 82, no. 12, pp. 1878–1880, 2003.
[64] G. Hahn, “Status of Selective Emitter Technology,” in *25th European Photovoltaic Solar Energy Conference and Exhibition / 5th World Conference on Photovoltaic Energy Conversion, 6-10 September 2010, Valencia, Spain*, Oct. 2010, pp. 1091–1096. doi: 10.4229/25thEUPVSEC2010-2DP.2.2.
[65] H. Wagner *et al.*, “Optimizing phosphorus diffusion for photovoltaic applications: Peak doping, inactive phosphorus, gettering, and contact formation,” *J. Appl. Phys.*, vol. 119, no. 18, pp. 185704–185704, 2016.
[66] K. H. Kim *et al.*, “Record high efficiency of screen-printed silicon aluminum back surface field solar cell: 20.29%,” *Jpn. J. Appl. Phys.*, vol. 56, no. 8, Aug. 2017, doi: 10.7567/JJAP.56.08MB25.
[67] B. Hoex, S. B. S. Heil, E. Langereis, M. C. M. Van De Banden, and W. M. M. Kessels, “Ultralow surface recombination of c-Si substrates passivated by plasma-assisted atomic layer deposited Al2O3,” *Appl. Phys. Lett.*, vol. 89, no. 4, 2006, doi: 10.1063/1.2240736.
[68] R. S. Bonilla, B. Hoex, P. Hamer, and P. R. Wilshaw, “Dielectric surface passivation for silicon solar cells: A review,” *Phys. Status Solidi A*, vol. 214, no. 7, pp. 1700293–1700293, 2017.
[69] M. A. Green, “The Passivated Emitter and Rear Cell (PERC): From conception to mass production,” *Sol. Energy Mater. Sol. Cells*, vol. 143, pp. 190–197, Dec. 2015, doi: 10.1016/j.solmat.2015.06.055.

[70] A. Blakers, “Development of the PERC solar cell,” *IEEE J. Photovolt.*, vol. 9, no. 3, pp. 629–635, 2019.
[71] M. Fischer, M. Woodhouse, S. Herritsch, and J. Trube, “International Technology Roadmap for Photovoltaic (ITRPV),” *VDMA EV*, vol. 12, Apr. 2021, [Online]. Available: https://itrpv.vdma.org/en/ueber-uns
[72] V. Shaw, “Trina announces 23.3% efficient PERC cell produced on commercial tools,” *PV magazine USA*, Mar. 05, 2020.
[73] H. Huang *et al.*, “20.8% industrial PERC solar cell: ALD Al2O3 rear surface passivation, efficiency loss mechanisms analysis and roadmap to 24%,” *Sol. Energy Mater. Sol. Cells*, vol. 161, pp. 14–30, 2017.
[74] B. Min *et al.*, “A roadmap toward 24% efficient PERC solar cells in industrial mass production,” *IEEE J. Photovolt.*, vol. 7, no. 6, pp. 1541–1550, Nov. 2017, doi: 10.1109/JPHOTOV.2017.2749007.
[75] M. Green, E. Dunlop, J. Hohl-Ebinger, M. Yoshita, N. Kopidakis, and X. Hao, “Solar cell efficiency tables (version 57),” *Prog. Photovolt. Res. Appl.*, vol. 29, no. 1, pp. 3–15, 2021, doi: https://doi.org/10.1002/pip.3371.
[76] A. Wang, J. Zhao, and M. A. Green, “24% efficient silicon solar cells,” *Appl. Phys. Lett.*, vol. 57, no. 6, pp. 602–604, Aug. 1990, doi: 10.1063/1.103610.
[77] J. Zhao, A. Wang, and M. A. Green, “24.5% Efficiency silicon PERT cells on MCZ substrates and 24.7% efficiency PERL cells on FZ substrates,” *Prog. Photovolt. Res. Appl.*, vol. 7, no. 6, pp. 471–474, 1999.
[78] M. D. Lammert and R. J. Schwartz, “The interdigitated back contact solar cell: A silicon solar cell for use in concentrated sunlight,” *IEEE Trans. Electron Devices*, vol. ED-24, no. 4, pp. 337–342, 1977, doi: 10.1109/T-ED.1977.18738.
[79] F. Haase *et al.*, “Laser contact openings for local poly-Si-metal contacts enabling 26.1%-efficient POLO-IBC solar cells,” *Sol. Energy Mater. Sol. Cells*, vol. 186, pp. 184–193, 2018.
[80] K. Yoshikawa *et al.*, “Silicon heterojunction solar cell with interdigitated back contacts for a photoconversion efficiency over 26%,” *Nat. Energy*, vol. 2, no. 5, pp. 17032–17032, Mar. 2017, doi: 10.1038/nenergy.2017.32.
[81] J. Nakamura, N. Asano, T. Hieda, C. Okamoto, H. Katayama, and K. Nakamura, “Development of heterojunction back contact Si solar cells,” *IEEE J. Photovolt.*, vol. 4, no. 6, pp. 1491–1495, Nov. 2014, doi: 10.1109/JPHOTOV.2014.2358377.
[82] A. Tomasi *et al.*, “Simple processing of back-contacted silicon heterojunction solar cells using selective-area crystalline growth,” *Nat. Energy*, vol. 2, no. 5, pp. 17062–17062, 2017.
[83] D. Lachenal *et al.*, “Optimization of tunnel-junction IBC solar cells based on a series resistance model,” *Sol. Energy Mater. Sol. Cells*, 2019, doi: 10.1016/j.solmat.2019.110036.
[84] Y. Chen *et al.*, “Mass production of industrial tunnel oxide passivated contacts (i-TOPCon) silicon solar cells with average efficiency over 23% and modules over 345 W,” *Prog. Photovolt. Res. Appl.*, Jul. 2019, doi: 10.1002/pip.3180.
[85] E. J. Charlson, A. B. Shah, and J. C. Lien, “A new silicon Schottky photovoltaic energy converter,” in *1972 International Electron Devices Meeting*, 1972, pp. 16–16.
[86] M. A. Green and A. W. Blakers, “Advantages of metal-insulator-semiconductor structures for silicon solar cells,” *Sol. Cells*, vol. 8, no. 1, pp. 3–16, 1983.
[87] A. Moldovan, F. Feldmann, M. Zimmer, J. Rentsch, J. Benick, and M. Hermle, “Tunnel oxide passivated carrier-selective contacts based on ultra-thin SiO2 layers,” *Sol. Energy Mater. Sol. Cells*, vol. 142, pp. 123–127, 2015.
[88] H. Kobayashi Asuha, O. Maida, M. Takahashi, and H. Iwasa, “Nitric acid oxidation of Si to form ultrathin silicon dioxide layers with a low leakage current density,” *J. Appl. Phys.*, vol. 94, no. 11, pp. 7328–7335, 2003.
[89] H. C. De Graaff and J. G. De Groot, “The SIS Tunnel Emitter: A Theory for Emitters with Thin Interface Layers,” *IEEE Trans. Electron Devices*, 1979, doi: 10.1109/T-ED.1979.19684.

[90] G. R. Wolstenholme, N. Jorgensen, P. Ashburn, and G. R. Booker, “An investigation of the thermal stability of the interfacial oxide in polycrystalline silicon emitter bipolar transistors by comparing device results with high-resolution electron microscopy observations,” *J. Appl. Phys.*, vol. 61, no. 1, pp. 225–233, 1987.

[91] J.-Y. Gan and R. M. Swanson, “Polysilicon emitters for silicon concentrator solar cells,” in *Photovoltaic Specialists Conference, 1990., Conference Record of the Twenty First IEEE*, 1990, pp. 245–250.

[92] D. Tetzlaff *et al.*, “A simple method for pinhole detection in carrier selective POLO-junctions for high efficiency silicon solar cells,” *Sol. Energy Mater. Sol. Cells*, vol. 173, pp. 106–110, 2017.

[93] B. Geerlings *et al.*, “LPCVD polysilicon passivating contacts for crystalline silicon solar cells,” *Photovolt. Int.*, vol. 32, pp. 45–56, 2016.

[94] D. Yan, A. Cuevas, S. P. Phang, Y. Wan, and D. Macdonald, “23% efficient p-type crystalline silicon solar cells with hole-selective passivating contacts based on physical vapor deposition of doped silicon films,” *Appl. Phys. Lett.*, vol. 113, no. 6, pp. 61603–61603, 2018.

[95] F. Feldmann, M. Bivour, C. Reichel, M. Hermle, and S. W. Glunz, “Passivated rear contacts for high-efficiency n-type Si solar cells providing high interface passivation quality and excellent transport characteristics,” *Sol. Energy Mater. Sol. Cells*, vol. 120, no. PART A, 2014, doi: 10.1016/j.solmat.2013.09.017.

[96] A. Richter *et al.*, “Design rules for high-efficiency both-sides-contacted silicon solar cells with balanced charge carrier transport and recombination losses,” *Nat. Energy*, vol. 6, no. 4, Art. no. 4, Apr. 2021, doi: 10.1038/s41560-021-00805-w.

[97] P. Padhamnath *et al.*, “Metal contact recombination in monoPoly^{TM} solar cells with screen-printed & fire-through contacts,” *Sol. Energy Mater. Sol. Cells*, vol. 192, pp. 109–116, Apr. 2019, doi: 10.1016/j.solmat.2018.12.026.

[98] D. Chen *et al.*, “24.58% total area efficiency of screen-printed, large area industrial silicon solar cells with the tunnel oxide passivated contacts (i-TOPCon) design,” *Sol. Energy Mater. Sol. Cells*, vol. 206, pp. 110258–110258, 2020, doi: 10.1016/j.solmat.2019.110258.

[99] M. Hutchin, “TOPCon technology hits 23.5% in mass production,” *pv magazine International*, Feb. 04, 2020. https://www.pv-magazine.com/2020/04/02/topcon-technology-hits-23-5-in-mass-production/ (accessed Feb. 16, 2021).

[100] L. Stoker, “LONGi toasts new p-type TOPCon and commercial heterojunction cell efficiency records,” *PV Tech*, Jun. 02, 2021. https://www.pv-tech.org/longi-toasts-new-p-type-topcon-and-commercial-heterojunction-cell-efficiency-records/ (accessed Jun. 28, 2021).

[101] Stoker, Liam, “N-type competition intensifying, industry transition could occur earlier than expected, says Jolywood,” *PV Tech*, Jun. 30, 2021. https://www.pv-tech.org/n-type-competition-intensifying-industry-transition-could-occur-earlier-than-expected-says-jolywood/ (accessed Jun. 30, 2021).

[102] A. G. Aberle, S. Glunz, and W. Warta, “Impact of illumination level and oxide parameters on Shockley–Read–Hall recombination at the Si-SiO2 interface,” *J. Appl. Phys.*, vol. 71, no. 9, pp. 4422–4431, 1992.

[103] F. Feldmann, M. Simon, M. Bivour, C. Reichel, M. Hermle, and S. W. Glunz, “Efficient carrier-selective p-and n-contacts for Si solar cells,” *Sol. Energy Mater. Sol. Cells*, vol. 131, pp. 100–104, 2014.

[104] G. Nogay *et al.*, “Interplay of annealing temperature and doping in hole selective rear contacts based on silicon-rich silicon-carbide thin films,” *Sol. Energy Mater. Sol. Cells*, vol. 173, 2017, doi: 10.1016/j.solmat.2017.06.039.

[105] P. Wyss *et al.*, “A mixed-phase SiOx hole helective junction compatible with high temperatures used in industrial solar cell manufacturing,” *IEEE J. Photovolt.*, pp. 1–8, 2020, doi: 10.1109/JPHOTOV.2020.3006979.

[106] A. Ingenito *et al.*, "A passivating contact for silicon solar cells formed during a single firing thermal annealing," *Nat. Energy*, vol. 3, no. 9, pp. 800–800, 2018.
[107] D. L. Young *et al.*, "Self-Aligned, Selective Area Poly-Si/SiO2 Passivated Contacts for Enhanced Photocurrent in Front/Back Solar Cells," National Renewable Energy Lab.(NREL), Golden, CO (United States), 2019.
[108] E. Bruhat, T. Desrues, D. Blanc-Pélissier, B. Martel, R. Cabal, and S. Dubois, "Contacting n+ Poly-Si Junctions with Fired AZO Layers: A Promising Approach for High Temperature Passivated Contact Solar Cells," in *2019 IEEE 46th Photovoltaic Specialists Conference (PVSC)*, 2019, pp. 2319–2324.
[109] J. Stuckelberger *et al.*, "Recombination Analysis of Phosphorus-Doped Nanostructured Silicon Oxide Passivating Electron Contacts for Silicon Solar Cells," *IEEE J. Photovolt.*, vol. 8, no. 2, 2018, doi: 10.1109/JPHOTOV.2017.2779871.
[110] Y. Larionova *et al.*, "On the recombination behavior of p+-type polysilicon on oxide junctions deposited by different methods on textured and planar surfaces," *Phys. Status Solidi A*, vol. 214, no. 8, pp. 1700058–1700058, 2017.
[111] K. Tool, M. Stodolny, J. Anker, G. Janssen, M. Lenes, and I. Romijn, "Miracle: Material Independent Rear Passivating Contact Solar cells using optimized texture and novel p+ poly-Si hydrogenation," in *2018 IEEE 7th World Conference on Photovoltaic Energy Conversion (WCPEC)(A Joint Conference of 45th IEEE PVSC, 28th PVSEC & 34th EU PVSEC)*, 2018, pp. 3900–3904.
[112] G. Nogay *et al.*, "Crystalline silicon solar cells with coannealed electron- and hole-selective SiCx passivating contacts," *IEEE J. Photovolt.*, vol. 8, no. 6, 2018, doi: 10.1109/JPHOTOV.2018.2866189.
[113] J. I. Pankove and M. L. Tarng, "Amorphous silicon as a passivant for crystalline silicon," *Appl. Phys. Lett.*, vol. 34, no. 2, pp. 156–157, 1979.
[114] M. Tanaka *et al.*, "Development of new a-Si/c-Si heterojunction solar cells: ACJ-HIT (Artificially Constructed Junction-Heterojunction with Intrinsic Thin-Layer)," *Jpn. J. Appl. Phys.*, vol. 31, no. Part 1, No. 11, pp. 3518–3522, Nov. 1992, doi: 10.1143/JJAP.31.3518.
[115] H. Keppner *et al.*, "Passivation properties of amorphous and microcrystalline silicon layers deposited by VHF-GD for crystalline silicon solar cells," *Sol. Energy Mater. Sol. Cells*, vol. 34, no. 1–4, pp. 201–209, Sep. 1994, doi: 10.1016/0927-0248(94)90041-8.
[116] M. Despeisse *et al.*, "Engineering of thin-film silicon materials for high efficiency crystalline silicon solar sells," in *2018 IEEE 7th World Conference on Photovoltaic Energy Conversion (WCPEC) (A Joint Conference of 45th IEEE PVSC, 28th PVSEC & 34th EU PVSEC)*, Jun. 2018, pp. 3888–3889. doi: 10.1109/PVSC.2018.8547369.
[117] K. Yoshikawa *et al.*, "Exceeding conversion efficiency of 26% by heterojunction interdigitated back contact solar cell with thin film Si technology," *Sol. Energy Mater. Sol. Cells*, 2017, doi: 10.1016/j.solmat.2017.06.024.
[118] A. Descoeudres *et al.*, "Low-temperature processes for passivation and metallization of high-efficiency crystalline silicon solar cells," *Sol. Energy*, vol. 175, no. January, pp. 54–59, 2018, doi: 10.1016/j.solener.2018.01.074.
[119] A. B. Morales-Vilches *et al.*, "ITO-free silicon heterojunction solar cells with ZnO:Al/SiO2 front electrodes reaching a conversion efficiency of 23%," *IEEE J. Photovolt.*, vol. 9, no. 1, pp. 34–39, 2018, doi: 10.1109/JPHOTOV.2018.2873307.
[120] A. Cuevas *et al.*, "Carrier population control and surface passivation in solar cells," *Sol. Energy Mater. Sol. Cells*, vol. 184, pp. 38–47, Sep. 2018, doi: 10.1016/J.SOLMAT.2018.04.026.
[121] M. Stutzmann, D. K. Biegelsen, and R. A. Street, "Detailed investigation of doping in hydrogenated amorphous silicon and germanium," *Phys. Rev. B*, vol. 35, no. 11, pp. 5666–5701, Apr. 1987, doi: 10.1103/PhysRevB.35.5666.

[122] M. Taguchi *et al.*, “HIT cells - high-efficiency crystalline Si cells with novel structure,” *Prog. Photovolt. Res. Appl.*, vol. 8, no. 5, pp. 503–513, Sep. 2000, doi: 10.1002/1099-159X(200009/10)8:5<503::AID-PIP347>3.0.CO;2-G.
[123] S. De Wolf and M. Kondo, “Nature of doped a-Si:H/c-Si interface recombination,” *J. Appl. Phys.*, vol. 105, no. 10, pp. 1–6, May 2009, doi: 10.1063/1.3129578.
[124] S. DeWolf *et al.*, “High-efficiency silicon heterojunction solar cells: A review,” *Green*, vol. 2, no. 1, pp. 7–24, 2012, doi: 10.1515/green-2011-0018.
[125] J.-W. A. Schüttauf, K. H. M. van der Werf, I. M. Kielen, W. G. J. H. M. van Sark, J. K. Rath, and R. E. I. Schropp, “Excellent crystalline silicon surface passivation by amorphous silicon irrespective of the technique used for chemical vapor deposition,” *Appl. Phys. Lett.*, vol. 98, no. 15, pp. 153514–153514, Apr. 2011, doi: 10.1063/1.3579540.
[126] U. K. Das, M. Z. Burrows, M. Lu, S. Bowden, and R. W. Birkmire, “Surface passivation and heterojunction cells on Si (100) and (111) wafers using DC and RF plasma deposited Si:H thin films,” *Appl. Phys. Lett.*, vol. 92, no. 6, 2008, doi: 10.1063/1.2857465.
[127] X. Zhang, A. Cuevas, B. Demaurex, and S. De Wolf, “Sputtered hydrogenated amorphous silicon for silicon heterojunction solar cell fabrication,” *Energy Procedia*, vol. 55, pp. 865–872, 2014, doi: 10.1016/j.egypro.2014.08.070.
[128] T. Koida, H. Fujiwara, and M. Kondo, “High-mobility hydrogen-doped In2 O3 transparent conductive oxide for a-Si:H/c-Si heterojunction solar cells,” *Solar Energy Materials And Solar Cells*, vol. 93, no. 6–7. Japan Soc Appl Phys; IEEE; Nagoya Ind Sci Res Inst, pp. 851–854, 2009. doi: 10.1016/j.solmat.2008.09.047.
[129] J. Yu *et al.*, “Tungsten doped indium oxide film: Ready for bifacial copper metallization of silicon heterojunction solar cell,” *Sol. Energy Mater. Sol. Cells*, vol. 144, pp. 359–363, 2015, doi: 10.1016/j.solmat.2015.09.033.
[130] E. Kobayashi, Y. Watabe, T. Yamamoto, and Y. Yamada, “Cerium oxide and hydrogen co-doped indium oxide films for high-efficiency silicon heterojunction solar cells,” *Sol. Energy Mater. Sol. Cells*, vol. 149, pp. 75–80, 2016, doi: 10.1016/j.solmat.2016.01.005.
[131] M. Morales-Masis *et al.*, “Highly Conductive and Broadband Transparent Zr-Doped In2O3 as Front Electrode for Solar Cells,” *IEEE J. Photovolt.*, vol. 8, no. 99, pp. 1202–1207, 2018.
[132] L.-L. Senaud *et al.*, “Aluminium-Doped Zinc Oxide Rear Reflectors for High-Efficiency Silicon Heterojunction Solar Cells,” *IEEE J. Photovolt.*, pp. 1–8, Aug. 2019, doi: 10.1109/jphotov.2019.2926860.
[133] J. Haschke, G. Christmann, C. Messmer, M. Bivour, M. Boccard, and C. Ballif, “Lateral Transport in Silicon Solar Cells,” *J. Appl. Phys.*, vol. 127, pp. 114501–114501, 2020, doi: 10.1063/1.5139416.
[134] J. L. Bryan *et al.*, “Aluminum-silicon interdiffusion in silicon heterojunction solar cells with a-Si:H(i)/a-Si:H(n/p)/Al rear contacts,” *J. Phys. Appl. Phys.*, Dec. 2020, doi: 10.1088/1361-6463/abd5e5.
[135] S. Li *et al.*, “Transparent-conductive-oxide-free front contacts for high-efficiency silicon heterojunction solar cells,” *Joule*, vol. 5, no. 6, pp. 1535–1547, Jun. 2021, doi: 10.1016/j.joule.2021.04.004.
[136] T. H. Ning and R. D. Isaac, “Effect of emitter contact on current gain of silicon bipolar devices,” *IEEE Trans. Electron Devices*, vol. 27, no. 11, pp. 2051–2055, 1980.
[137] Z. C. Holman *et al.*, “Current losses at the front of silicon heterounction solar cells,” *IEEE J. Photovolt.*, vol. 2, no. No. 1, 2012, doi: 10.1109/JPHOTOV.2011.2174967.
[138] M. W. M. M. van Cleef, F. A. Rubinelli, R. Rizzoli, R. Pinghini, R. E. I. I. Schropp, and W. F. Van Der Weg, “Amorphous silicon carbide/crystalline silicon heterojunction solar cells: a comprehensive study of the photocarrier collection,” *Jpn. J. Appl. Phys.*, vol. 37, no. 7R, pp. 3926–3926, 1998.

[139] S. Kirner, L. Mazzarella, L. Korte, B. Stannowski, B. Rech, and R. Schlatmann, “Silicon heterojunction solar cells with nanocrystalline silicon oxide emitter: Insights into charge carrier transport,” *IEEE J. Photovolt.*, 2015, doi: 10.1109/JPHOTOV.2015.2479461.
[140] J. P. Seif *et al.*, “Nanometer-scale doped microcrystalline silicon Layers for silicon heterojunction solar cells,” 2015.
[141] G. Nogay *et al.*, “Microcrystalline silicon carrier collectors for silicon heterojunction solar cells and impact on low-temperature device characteristics,” *2017 IEEE 44th Photovolt. Spec. Conf. PVSC 2017*, vol. 6, no. 6, pp. 1–3, 2017, doi: 10.1109/PVSC.2017.8366840.
[142] L. Mazzarella *et al.*, “Nanocrystalline silicon emitter optimization for Si-HJ solar cells: Substrate selectivity and CO2 plasma treatment effect,” *Phys. Status Solidi Appl. Mater. Sci.*, 2017, doi: 10.1002/pssa.201532958.
[143] A. N. Fioretti, M. Boccard, R. Monnard, and C. Ballif, “Low-temperature p-type microcrystalline silicon as carrier selective contact for silicon heterojunction solar cells,” *IEEE J. Photovolt.*, vol. PP, pp. 1–8, 2019, doi: 10.1109/JPHOTOV.2019.2917550.
[144] M. Bivour, J. Temmler, H. Steinkemper, and M. Hermle, “Molybdenum and tungsten oxide: High work function wide band gap contact materials for hole selective contacts of silicon solar cells,” *Sol. Energy Mater. Sol. Cells*, vol. 142, pp. 34–41, 2015, doi: 10.1016/j.solmat.2015.05.031.
[145] A. S. Gudovskikh *et al.*, “Study of GaP/Si heterojunction solar cells,” *Energy Procedia*, vol. 102, pp. 56–63, Dec. 2016, doi: 10.1016/j.egypro.2016.11.318.
[146] M. Glatthaar, I. Kafedjiska, M. Bivour, and S. Hopman, “Self-aligned PEDOT:PSS contacts on highly transparent boron emitters,” *Sol. Energy Mater. Sol. Cells*, vol. 173, p. 92.95-92.95, 2017.
[147] J. Bullock *et al.*, “Stable dopant-free asymmetric heterocontact silicon solar cells with efficiencies above 20%,” *ACS Energy Lett.*, vol. 3, no. 3, pp. 508–513, Mar. 2018, doi: 10.1021/acsenergylett.7b01279.
[148] S. Essig *et al.*, “Toward annealing-stable molybdenum-oxide-based hole-selective contacts for silicon photovoltaics,” *Sol. RRL*, vol. 2, no. 4, pp. 1700227–1700227, Feb. 2018, doi: 10.1002/solr.201700227.
[149] J. Melskens, B. W. H. van de Loo, B. Macco, L. E. Black, S. Smit, and W. M. M. Kessels, “Passivating contacts for crystalline silicon solar cells: From concepts and materials to prospects,” *IEEE J. Photovolt.*, vol. 8, no. 2, pp. 373–388, Mar. 2018, doi: 10.1109/JPHOTOV.2018.2797106.
[150] X. Yang *et al.*, “Dual-function electron-conductive, hole-blocking titanium nitride contacts for efficient silicon solar cells,” *Joule*, vol. 3, no. 5, pp. 1314–1327, 2019, doi: 10.1016/j.joule.2019.03.008.
[151] X. Yang, Q. Bi, H. Ali, K. Davis, W. V. Schoenfeld, and K. Weber, “High-performance TiO2-based electron-selective contacts for crystalline silicon solar cells,” *Adv. Mater.*, pp. 5891–5897, 2016, doi: 10.1002/adma.201600926.
[152] J. Dréon *et al.*, “23.5%-efficient silicon heterojunction silicon solar cell using molybdenum oxide as hole-selective contact,” *Nano Energy*, vol. 70, p. 104495, 2020.
[153] J. Bullock *et al.*, “Dopant-free partial rear contacts enabling 23% silicon solar cells,” *Adv. Energy Mater.*, pp. 1803367–1803367, Jan. 2019, doi: 10.1002/aenm.201803367.
[154] W. Wu *et al.*, “22% efficient dopant-free interdigitated back contact silicon solar cells,” in *AIP Conference Proceedings*, 2018, vol. 1999, no. 1, pp. 40025–40025.
[155] S. Zhong *et al.*, “Mitigating plasmonic absorption losses at rear electrodes in high-efficiency silicon solar cells using dopant-free contact stacks,” *Adv. Functinal Mater.*.
[156] A. Paduthol, M. K. Juhl, G. Nogay, P. Löper, A. Ingenito, and T. Trupke, “Impact of different capping layers on carrier injection efficiency between amorphous and crystalline silicon measured using photoluminescence,” *Sol. Energy Mater. Sol. Cells*, vol. 187, no. July, pp. 55–60, 2018, doi: 10.1016/j.solmat.2018.07.016.

[157] K. Masuko *et al.*, “Achievement of more than 25% conversion efficiency with crystalline silicon heterojunction solar cell,” *IEEE J. Photovolt.*, vol. 4, no. 6, pp. 1433–1435, 2014.
[158] M. Boccard and Z. C. Holman, “Amorphous silicon carbide passivating layers for crystalline-silicon-based heterojunction solar cells,” *J. Appl. Phys.*, vol. 118, no. 6, 2015, doi: 10.1063/1.4928203.
[159] A. Defresne, O. Plantevin, and P. Roca i Cabarrocas, “Robustness up to 400°C of the passivation of c-Si by p-type a-Si:H thanks to ion implantation,” *AIP Adv.*, vol. 6, no. 12, pp. 125107–125107, Dec. 2016, doi: 10.1063/1.4971276.
[160] J. Shi, M. Boccard, and Z. Holman, “Plasma-initiated rehydrogenation of amorphous silicon to increase the temperature processing window of silicon heterojunction solar cells,” *Appl. Phys. Lett.*, vol. 109, no. 3, 2016, doi: 10.1063/1.4958831.
[161] J. Geissbühler, “Metallization techniques and interconnection schemes for high efficiency silicon heterojunction PV,” *Photovolt. Int.*, vol. 37, pp. 67–67, 2017.
[162] B. A. Kamino *et al.*, “Low-temperature screen-printed metallization for the scale-up of two-terminal perovskite–silicon tandems,” *ACS Appl. Energy Mater.*, p. acsaem.9b00502-acsaem.9b00502, May 2019, doi: 10.1021/acsaem.9b00502.
[163] M. M. Kivambe *et al.*, “Record-efficiency n-type and high-efficiency p-type monolike silicon heterojunction solar cells with a high-temperature gettering process,” *ACS Appl. Energy Mater.*, p. acsaem.9b00608-acsaem.9b00608, Jul. 2019, doi: 10.1021/acsaem.9b00608.
[164] S. Harrison and others, “How to deal with thin wafers in aheterojunction solar cells industial pilot line: First analyses of the integration of cells to 70 µm thick in production mode,” *Proceeding 32th EU PVSEC Ger.*, pp. 358–362, 2016.
[165] A. Augusto, E. Looney, C. Del Cañizo, S. G. Bowden, and T. Buonassisi, “Thin silicon solar cells: Pathway to cost-effective and defect-tolerant cell design,” *Energy Procedia*, vol. 124, pp. 706–711, 2017, doi: 10.1016/j.egypro.2017.09.346.
[166] A. Descoeudres, Z. C. Holman, L. Barraud, S. Morel, S. De Wolf, and C. Ballif, “>21% efficient silicon heterojunction solar cells on n-and p-type wafers compared,” *IEEE J. Photovolt.*, vol. 3, no. 1, pp. 83–89, 2013.
[167] J. Zhao *et al.*, “24% silicon heterojunction solar cells on Meyer Burger’s mass production tools and how wafer material impacts cell parameters,” in *2018 IEEE 7th World Conference on Photovoltaic Energy Conversion, WCPEC 2018 - A Joint Conference of 45th IEEE PVSC, 28th PVSEC and 34th EU PVSEC*, Jun. 2018, pp. 1514–1519. doi: 10.1109/PVSC.2018.8547908.
[168] O. Dupré, J. Levrat, J. Champliaud, M. Despeisse, M. Boccard, and C. Ballif, “Reassessment of cell to module gains and losses: Accounting for the current boost specific to cells located on the edges,” in *AIP Conference Proceedings*, 2018, vol. 1999, no. 1, pp. 90001–90001.
[169] P. Papet *et al.*, “New Cell Metallization Patterns for Heterojunction Solar Cells Interconnected by the Smart Wire Connection Technology,” *Energy Procedia*, vol. 67, pp. 203–209, Apr. 2015, doi: 10.1016/J.EGYPRO.2015.03.039.
[170] S. Braun, G. Hahn, R. Nissler, C. Pönisch, and D. Habermann, “The multi-busbar design: An overview,” *Energy Procedia*, vol. 43, pp. 86–92, Jan. 2013, doi: 10.1016/J.EGYPRO.2013.11.092.
[171] A. Faes *et al.*, “Direct contact to TCO with SmartWire connection technology,” in *2018 IEEE 7th World Conference on Photovoltaic Energy Conversion (WCPEC)*, Jun. 2018, pp. 1998–2001. doi: 10.1109/PVSC.2018.8547406.
[172] J. D. C. Dickson, “Photo-voltaic semiconductor apparatus or the like,” 1960
[173] J. Zhao, A. Wang, E. Abbaspour-Sani, F. Yun, and M. A. Green, “Improved efficiency silicon solar cell module,” *IEEE Electron Device Lett.*, vol. 18, no. 2, pp. 48–50, Feb. 1997, doi: 10.1109/55.553040.
[174] A. J. Carr *et al.*, “Tessera: Scalable, shade robust module,” in *2015 IEEE 42nd Photovoltaic Specialist Conference (PVSC)*, 2015, pp. 1–5.

[175] F. Gérenton *et al.*, “Silicon heterojunction and half-cell configuration: optimization path for increased module power,” 2019.
[176] S. K. Chunduri, “Advanced Module Technologies 2019 | TaiyangNews,” 2019. [Online]. Available: http://taiyangnews.info/reports/advanced-module-technologies-2019/
[177] P. Baliozian, E. Lohmüller, T. Fellmeth, N. Wöhrle, A. Krieg, and R. Preu, “Bifacial p-type silicon shingle solar cells − the ‘pSPEER’ concept,” *Sol. RRL*, vol. 2, no. 3, pp. 1700171–1700171, Mar. 2018, doi: 10.1002/solr.201700171.
[178] N. Klasen, A. Mondon, A. Kraft, and U. Eitner, “Shingled cell interconnection: A new generation of bifacial PV-modules,” *SSRN Electron. J.*, Apr. 2018, doi: 10.2139/ssrn.3152478.
[179] J. Park, W. Oh, H. Park, C. Jeong, B. Choi, and J. Lee, “Analysis of solar cells interconnected by electrically conductive adhesives for high-density photovoltaic modules,” *Appl. Surf. Sci.*, 2019, doi: 10.1016/j.apsusc.2019.03.307.
[180] H. Schulte-Huxel, S. Blankemeyer, A. Morlier, R. Brendel, and M. Köntges, “Interconnect-shingling: Maximizing the active module area with conventional module processes,” *Sol. Energy Mater. Sol. Cells*, 2019, doi: 10.1016/j.solmat.2019.109991.
[181] C. Ballif, J. Dicker, D. Borchert, and T. Hofmann, “Solar glass with industrial porous SiO2 antireflection coating: measurements of photovoltaic module properties improvement and modelling of yearly energy yield gain,” *Sol. Energy Mater. Sol. Cells*, vol. 82, no. 3, pp. 331–344, 2004.
[182] X. Pan, S. Zhang, J. Xu, Z. Feng, and P. J. Verlinden, “Performance of Different Anti-Reflective Coated Glass for PV Modules,” *Proc 31st EU PVSEC*, 2015.
[183] S. Zhang *et al.*, “335-W world-record p-type monocrystalline module with 20.6% efficient PERC solar cells,” *IEEE J. Photovolt.*, vol. 6, no. 1, pp. 145–152, 2015.
[184] S. Pingel *et al.*, “Potential Induced Degradation of solar cells and panels,” in *2010 35th IEEE Photovoltaic Specialists Conference*, Jun. 2010, pp. 002817–002822. doi: 10.1109/PVSC.2010.5616823.
[185] V. Naumann *et al.*, “Explanation of potential-induced degradation of the shunting type by Na decoration of stacking faults in Si solar cells,” *Sol. Energy Mater. Sol. Cells*, vol. 120, pp. 383–389, 2014.
[186] A. Virtuani, E. Annigoni, and C. Ballif, “One-type-fits-all-systems: Strategies for preventing potential-induced degradation in crystalline silicon solar photovoltaic modules,” *Prog. Photovolt. Res. Appl.*, vol. 27, no. 1, pp. 13–21, 2019.
[187] J. H. Wohlgemuth, *Photovoltaic Module Reliability*. John Wiley & Sons, 2020.
[188] D. C. Jordan, S. R. Kurtz, K. VanSant, and J. Newmiller, “Compendium of photovoltaic degradation rates,” *Prog. Photovolt. Res. Appl.*, vol. 24, no. 7, pp. 978–989, Jul. 2016, doi: 10.1002/pip.2744.
[189] M. Schweiger, J. Bonilla, W. Herrmann, A. Gerber, and U. Rau, “Performance stability of photovoltaic modules in different climates,” *Prog. Photovolt. Res. Appl.*, vol. 25, no. 12, pp. 968–981, 2017, doi: 10.1002/pip.2904.
[190] T. Ishii and A. Masuda, “Annual degradation rates of recent crystalline silicon photovoltaic modules,” *Prog. Photovolt. Res. Appl.*, vol. 25, no. 12, pp. 953–967, 2017, doi: 10.1002/pip.2903.
[191] F. Carigiet, C. J. Brabec, and F. P. Baumgartner, “Long-term power degradation analysis of crystalline silicon PV modules using indoor and outdoor measurement techniques,” *Renew. Sustain. Energy Rev.*, vol. 144, p. 111005, Jul. 2021, doi: 10.1016/j.rser.2021.111005.
[192] S. Yamaguchi, C. Yamamoto, K. Ohdaira, and A. Masuda, “Comprehensive study of potential-induced degradation in silicon heterojunction photovoltaic cell modules,” *Prog. Photovolt. Res. Appl.*, vol. 26, no. 9, pp. 697–708, 2018, doi: 10.1002/pip.3006.
[193] O. Arriaga Arruti, L. Gnocchi, A. Virtuani, and C. Ballif, “Encapsulant Selection for PID Resistant Modules Made with Heterojunction Solar Cells,” *37th Eur. Photovolt. Sol. Energy Conf. Exhib.*, pp. 974–977, Oct. 2020, doi: 10.4229/EUPVSEC20202020-4AV.1.8.

[194] J. Cattin *et al.*, “Influence of Light Soaking on Silicon Heterojunction Solar Cells With Various Architectures,” *IEEE J. Photovolt.*, vol. 11, no. 3, pp. 575–583, May 2021, doi: 10.1109/JPHOTOV.2021.3065537.
[195] A. Virtuani *et al.*, “35 years of photovoltaics: Analysis of the TISO-10-kW solar plant, lessons learnt in safety and performance—Part 1,” *Prog. Photovolt. Res. Appl.*, vol. 27, no. 4, pp. 328–339, Apr. 2019, doi: 10.1002/pip.3104.
[196] A. Richter, “System design, optimization and performance energy yield of bifacial module technologies and yield estimation methods by rule of thumb,” 2018.
[197] R. Kopecek and J. Libal, *Bifacial photovoltaics: Technology, applications and economics*. Institution of Engineering and Technology, 2018.
[198] R. Kopecek and J. Libal, “Towards large-scale deployment of bifacial photovoltaics,” *Nat. Energy*, vol. 3, no. 6, pp. 443–446, Jun. 2018, doi: 10.1038/s41560-018-0178-0.
[199] T. Heggarty, “Global Solar Installations to Reach Record High in 2019,” *Greentech media*, Jul. 25, 2019. Accessed: Aug. 30, 2019. [Online]. Available: https://www.greentechmedia.com/articles/read/global-solar-pv-installations-to-reach-record-high-in-2019#gs.zztl38
[200] J. Deign, “Mexican Solar Sets a Record Low Price for Latin America,” *Greentech Media*, Nov. 29, 2017. Accessed: Aug. 30, 2019. [Online]. Available: https://www.greentechmedia.com/articles/read/mexican-solar-record-low-price-latin-america#gs.zztcyw
[201] A. Di Paola, “Saudi Arabia Gets Cheapest Bids for Solar Power in Auction,” *Bloomberg*, Oct. 03, 2017. Accessed: Aug. 30, 2019. [Online]. Available: https://www.bloomberg.com/news/articles/2017-10-03/saudi-arabia-gets-cheapest-ever-bids-for-solar-power-in-auction
[202] N. M. Haegel *et al.*, “Terawatt-scale photovoltaics: Transform global energy,” *Science*, vol. 364, no. 6443, pp. 836–838, 2019.
[203] C. Breyer *et al.*, “On the role of solar photovoltaics in global energy transition scenarios,” *Prog. Photovolt. Res. Appl.*, vol. 25, no. 8, pp. 727–745, 2017.
[204] P. J. Verlinden, “Future challenges for photovoltaic manufacturing at the terawatt level,” *J. Renew. Sustain. Energy*, vol. 12, no. 5, 2020, doi: 10.1063/5.0020380.
[205] P. P. Altermatt *et al.*, “Requirements of the Paris Climate Agreement for the coming 10 years on investments, technical roadmap, and expansion of PV manufacturing,” p. 31. doi: 10.4229/EUPVSEC20202020-7CP.1.2.
[206] Y. Chen *et al.*, “From laboratory to production: Learning models of efficiency and manufacturing cost of industrial crystalline silicon and thin-film photovoltaic technologies,” *IEEE J. Photovolt.*, vol. 8, no. 6, pp. 1531–1538, Nov. 2018, doi: 10.1109/JPHOTOV.2018.2871858.
[207] K. Zweibel, “The impact of tellurium supply on cadmium telluride photovoltaics,” *Science*, vol. 328, no. 5979, pp. 699–701, May 2010, doi: 10.1126/science.1189690.
[208] A. Vijh, L. Washington, and R. C. Parenti, “High performance, lightweight GaAs solar cells for aerospace and mobile applications,” in *2017 IEEE 44th Photovoltaic Specialist Conference (PVSC)*, 2017, pp. 3520–3523. doi: 10.1109/PVSC.2017.8366342.
[209] S. Essig *et al.*, “Raising the one-sun conversion efficiency of III–V/Si solar cells to 32.8% for two junctions and 35.9% for three junctions,” *Nat. Energy*, vol. 2, no. 9, pp. 17144–17144, Aug. 2017, doi: 10.1038/nenergy.2017.144.
[210] R. Cariou *et al.*, “III-V-on-silicon solar cells reaching 33% photoconversion efficiency in two-terminal configuration,” *Nat. Energy*, vol. 3, no. 4, pp. 326–333, Apr. 2018, doi: 10.1038/s41560-018-0125-0.
[211] S. Fan *et al.*, “Current-Matched III–V/Si Epitaxial Tandem Solar Cells with 25.0% Efficiency,” *Cell Rep. Phys. Sci.*, vol. 1, no. 9, p. 100208, Sep. 2020, doi: 10.1016/j.xcrp.2020.100208.

[212] M. Feifel *et al.*, “Epitaxial GaInP/GaAs/Si Triple-Junction Solar Cell with 25.9% AM1.5g Efficiency Enabled by Transparent Metamorphic AlxGa1−xAsyP1−y Step-Graded Buffer Structures,” *Sol. RRL*, vol. 5, no. 5, p. 2000763, 2021, doi: 10.1002/solr.202000763.
[213] K. A. Bush *et al.*, “Minimizing current and voltage losses to reach 25% efficient monolithic two-terminal perovskite-silicon tandem solar cells,” *ACS Energy Lett.*, vol. 3, no. 9, pp. 2173–2180, Sep. 2018, doi: 10.1021/acsenergylett.8b01201.
[214] F. Sahli *et al.*, “Fully textured monolithic perovskite/silicon tandem solar cells with 25.2% power conversion efficiency,” *Nat. Mater.*, vol. 17, no. 9, pp. 820–820, Jun. 2018, doi: 10.1038/s41563-018-0115-4.
[215] B. Chen *et al.*, “Grain engineering for perovskite/silicon monolithic tandem solar cells with efficiency of 25.4%,” *Joule*, vol. 3, no. 1, pp. 177–190, Jan. 2019, doi: 10.1016/j.joule.2018.10.003.
[216] L. Mazzarella *et al.*, “Infrared light management using a nanocrystalline silicon oxide interlayer in monolithic perovskite/silicon heterojunction tandem solar cells with efficiency above 25%,” *Adv. Energy Mater.*, vol. 9, no. 14, Apr. 2019, doi: 10.1002/aenm.201803241.
[217] A. Al-Ashouri *et al.*, “Monolithic perovskite/silicon tandem solar cell with >29% efficiency by enhanced hole extraction,” *Science*, vol. 370, no. 6522, pp. 1300–1309, Dec. 2020, doi: 10.1126/science.abd4016.
[218] M. A. Green, E. D. Dunlop, J. Hohl-Ebinger, M. Yoshita, N. Kopidakis, and X. Hao, “Solar cell efficiency tables (Version 58),” *Prog. Photovolt. Res. Appl.*, vol. 29, no. 7, pp. 657–667, 2021, doi: 10.1002/pip.3444.
[219] M. Hutchins, “A 26.5% efficient perovskite-silicon tandem cell,” *pv magazine International*, Dec. 2020. https://www.pv-magazine.com/2020/12/09/a-26-5-efficient-perovskite-silicon-tandem-cell/ (accessed Jul. 05, 2021).
[220] J. Werner, B. Niesen, and C. Ballif, “Perovskite/silicon tandem solar cells: Marriage of convenience or true love story?–An overview,” *Adv. Mater. Interfaces*, vol. 5, no. 1, p. 1700731, 2018.
[221] A. Descoeudres *et al.*, “The versatility of passivating carrier-selective silicon thin films for diverse high-efficiency screen-printed heterojunction-based solar cells,” *Prog. Photovolt. Res. Appl.*, no. November, pp. 1–9, 2019, doi: 10.1002/pip.3227.
[222] D. D. Smith, G. Reich, M. Baldrias, M. Reich, N. Boitnott, and G. Bunea, “Silicon solar cells with total area efficiency above 25 %,” in *2016 IEEE 43rd Photovoltaic Specialists Conference (PVSC)*, 2016, pp. 3351–3355. doi: 10.1109/PVSC.2016.7750287.
[223] “LONGi breaks world record for HJT solar cell efficiency twice in one week.” https://en.longi-solar.com/home/events/press_detail/id/364_LONGi_breaks_world_record_for_HJT_solar_cell_efficiency_twice_in_one_week.html (accessed Jan. 05, 2022).
[224] K. Yamamoto *et al.*, “Progress & Challenges in Thin-Film Silicon Photovoltaics: Heterojunctions & Multijunctions,” in *Proc. 31st Eur. Photovolt. Sol. Energy Conf. Exhib.*, 2015, p. 3CP.1.1-3CP.1.1.
[225] A. Richter, J. Benick, F. Feldmann, A. Fell, M. Hermle, and S. W. Glunz, “n-Type Si solar cells with passivating electron contact: Identifying sources for efficiency limitations by wafer thickness and resistivity variation,” *Sol. Energy Mater. Sol. Cells*, vol. 173, pp. 96–105, 2017.
[226] S. W. Glunz and F. Feldmann, “SiO2 surface passivation layers – a key technology for silicon solar cells,” *Sol. Energy Mater. Sol. Cells*, 2018, doi: 10.1016/j.solmat.2018.04.029.
[227] Q. Wang, “Status of Crystalline Silicon PERC Solar Cells,” presented at the NIST/UL Workshop on Photovoltaic Material Durability, NIST Gaithersburg MD, USA, Dec. 12, 2019.
[228] F. Stenzel *et al.*, “Exceeding 23% and mass production of P-Cz Q.ANTUM bifacial solar cells,” 2019.
[229] J. W. Müller *et al.*, “Approaching 24% cell efficiency in mass production,” presented at the 30th Int. PVSEC, Jeju Island, Korea.

[230] T. Guoqiang, C. Cong, C. Yifang, Z. Bing, C. Yanguo, and W. Tihu, “Numerical Simulations of a 96-rod Polysilicon CVD Reactor,” *J. Cryst. Growth*, vol. 489, pp. 68–71, May 2018, doi: 10.1016/j.jcrysgro.2018.01.007.
[231] P. P. Altermatt, G. Xu, X. Zhang, D. Chen, Y. Chen, and Z. Feng, “From upscaling PERC to the next technology cycle: transparent passivating contacts may merger n- and p-type cell technology,” in *Proc. 38th European PVSEC*, 2021, p. 2AO.8.1.
[232] S. Philipps and W. Warmuth, “Fraunhofer ISE: Photovoltaics Report, updated: September 2020,” 2020. [Online]. Available: https://www.ise.fraunhofer.de/en/publications/studies/photovoltaics-report.html
[233] A. Graf, A. Herguth, and G. Hahn, “Determination of BO-LID and LeTID related activation energies in Cz-Si and FZ-Si using constant injection conditions,” *AIP Conf. Proc.*, vol. 2147, no. 1, p. 140003, Aug. 2019, doi: 10.1063/1.5123890.
[234] S. Joos and G. Hahn, “Marktführer mit Zukunft: Industrielle Herstellung von Silizium-Solarzellen,” *Phys. Unserer Zeit*, vol. 47, no. 5, pp. 240–246, 2016.
[235] S. Gatz *et al.*, “19.4%-efficient large-area fully screen-printed silicon solar cells,” *Phys. Status Solidi - Rapid Res. Lett.*, 2011, doi: 10.1002/pssr.201105045.
[236] E. Christensen, *Flat-Plate Solar Array Project of the US Department of Energy’s National Photovoltaics Program: 10 Years of Progress*, no. 400. Jet Propulsion Laboratory, 1985.
[237] A. W. Blakers and M. A. Green, “20% efficiency silicon solar cells,” *Appl. Phys. Lett.*, vol. 48, no. 3, pp. 215–217, 1986, doi: 10.1063/1.96799.
[238] P. Verlinden, R. A. Sinton, and R. M. Swanson, “High efficiency large area back contact concentrator solar cells with a multilevel interconnection,” *Int. J. Sol. Energy*, vol. 6, no. 6, pp. 347–366, Jan. 1988, doi: 10.1080/01425918808914239.
[239] P. A. Basore and J. M. Gee, “Crystalline-silicon photovoltaics: necessary and sufficient,” in *Proceedings of 1994 IEEE 1st World Conference on Photovoltaic Energy Conversion - WCPEC (A Joint Conference of PVSC, PVSEC and PSEC)*, 1994, vol. 2, pp. 2254–2257. doi: 10.1109/WCPEC.1994.521674.
[240] M. A. Green, “How did solar cells get so cheap?,” *Joule*, vol. 3, no. 3, pp. 631–633, Mar. 2019, doi: 10.1016/j.joule.2019.02.010.
[241] Y. M. Yang, A. Yu, B. Hsu, W. C. Hsu, A. Yang, and C. W. Lan, “Development of high-performance multicrystalline silicon for photovoltaic industry,” *Prog. Photovolt. Res. Appl.*, vol. 23, no. 3, pp. 340–351, Mar. 2015, doi: 10.1002/pip.2437.
[242] C. W. Lan *et al.*, “The emergence of high-performance multi-crystalline silicon in photovoltaics,” *J. Cryst. Growth*, vol. 468, pp. 17–23, 2017.
[243] N. Stoddard *et al.*, “Casting single crystal silicon: Novel defect profiles from BP Solar’s mono2 TM wafers,” *Solid State Phenom.*, vol. 131–133, pp. 1–8, Oct. 2007, doi: 10.4028/www.scientific.net/ssp.131-133.1.
[244] C.-W. Lan, C.-K. Hsieh, and W.-C. Hsu, “Czochralski silicon crystal growth for photovoltaic applications,” in *Crystal growth of Si for solar cells*, Springer, 2009, pp. 25–39.
[245] H. Xu, “Characterization of n-type mono-crystalline silicon ingots produced by continuous Czochralski (Cz) Technology,” *Energy Procedia*, vol. 77, pp. 658–664, 2015.
[246] Y. Wang, T. Xie, L. Green, and X. City, “Supply of low-cost and high-efficiency multi-GW mono wafers,” *Photovolt. Int.*, vol. 36, pp. 38–42, 2017.
[247] F. Mosel *et al.*, “Cost Effective Growth of Silicon Mono Ingots by the Application of a Mobile Recharge System in CZ-Puller,” in *32nd EU-PVSEC*, 2016, pp. 1064–1068.
[248] R. Brendel, “Review of layer transfer processes for crystalline thin-film silicon solar cells,” *Jpn. J. Appl. Phys.*, vol. 40, no. 7R, pp. 4431–4431, 2001.
[249] N. Milenkovic, M. Drießen, C. Weiss, and S. Janz, “Porous silicon reorganization: Influence on the structure, surface roughness and strain,” *J. Cryst. Growth*, vol. 432, pp. 139–145, 2015.
[250] G. Hahn and A. Schönecker, “New crystalline silicon ribbon materials for photovoltaics,” *J. Phys. Condens. Matter*, vol. 16, no. 50, pp. R1615–R1615, 2004.

[251] F. Van Mierlo, R. Jonczyk, and V. Qian, “Next generation Direct Wafer® technology delivers low cost, high performance to silicon wafer industry,” in *Energy Procedia*, 2017, vol. 130, pp. 2–6. doi: 10.1016/j.egypro.2017.09.403.
[252] W. Shockley and H. J. Queisser, “Detailed balance limit of efficiency of p-n junction solar cells,” *J. Appl. Phys.*, vol. 32, no. 3, pp. 510–519, 1961, doi: 10.1063/1.1736034.
[253] R. M. Swanson, “Approaching the 29% limit efficiency of silicon solar cells,” in *Conference Record of the Thirty-first IEEE Photovoltaic Specialists Conference, 2005.*, 2005, pp. 889–894.
[254] A. Richter, M. Hermle, and S. W. Glunz, “Reassessment of the Limiting Efficiency for Crystalline Silicon Solar Cells,” *IEEE J. Photovolt.*, vol. 3, no. 4, pp. 1184–1191, 2013, doi: 10.1109/JPHOTOV.2013.2270351.
[255] B. A. Veith-Wolf, S. Schäfer, R. Brendel, and J. Schmidt, “Reassessment of intrinsic lifetime limit in n-type crystalline silicon and implication on maximum solar cell efficiency,” *Sol. Energy Mater. Sol. Cells*, vol. 186, pp. 194–199, 2018.
[256] M. J. Kerr and A. Cuevas, “General parameterization of Auger recombination in crystalline silicon,” *J. Appl. Phys.*, vol. 91, no. 4, pp. 2473–2480, 2002.
[257] S. Schäfer and R. Brendel, “Accurate calculation of the absorptance enhances efficiency limit of crystalline silicon solar cells with lambertian light trapping,” *IEEE J. Photovolt.*, vol. 8, no. 4, pp. 1156–1158, 2018.